

1   **Adhesion-based capture stabilizes nascent microvilli at**  
2   **epithelial cell junctions**

3

4   Caroline S. Cencer<sup>1</sup>, Jennifer B. Silverman<sup>1</sup>, Leslie M. Meenderink<sup>1</sup>, Evan S. Krystofiak<sup>1</sup>,  
5   Bryan A. Millis<sup>2</sup>, and Matthew J. Tyska<sup>1,3</sup>

6

7   <sup>1</sup>Department of Cell and Developmental Biology  
8   Vanderbilt University School of Medicine  
9   Nashville, TN 37232

10

11   <sup>2</sup>Department of Biomedical Engineering  
12   Vanderbilt University School of Engineering  
13   Nashville, TN 37235

14

15   <sup>3</sup>Lead Contact

16

17   **Keywords:** transporting epithelia, actin, cadherins, differentiation, brush border,  
18   intermicrovillar adhesion

19

20   **Word count:** 6,565 words (includes Introduction, Results, Discussion, Figure Legends)

21

22   **To whom correspondence should be addressed:**

23   Matthew J. Tyska, Ph.D.

24   Department of Cell and Developmental Biology

25   Vanderbilt University School of Medicine

26   T-2212 Medical Center North

27   465 21<sup>st</sup> Avenue South

28   Nashville, TN 37240-7935

29   Office: 615-936-5461

30   Email: matthew.tyska@vanderbilt.edu

31 **SUMMARY**

32 Differentiated transporting epithelial cells present an extensive apical array of microvilli –  
33 a “brush border” – where neighboring microvilli are linked together by intermicrovillar  
34 adhesion complexes (IMACs) composed of protocadherins CDHR2 and CDHR5.  
35 Although loss-of-function studies provide strong evidence that IMAC function is needed  
36 to build a mature brush border, how the IMAC contributes to the stabilization and  
37 accumulation of nascent microvilli remains unclear. We found that, early in differentiation,  
38 the apical surface exhibits a marginal accumulation of microvilli, characterized by higher  
39 packing density relative to medial regions of the surface. While medial microvilli are highly  
40 dynamic and sample multiple orientations over time, marginal protrusions exhibit  
41 constrained motion and maintain a vertical orientation. Unexpectedly, we found that  
42 marginal microvilli span the junctional space and contact protrusions on neighboring cells,  
43 mediated by complexes of CDHR2/CDHR5. FRAP analysis indicated that these  
44 *transjunctional* IMACs are highly stable relative to adhesion complexes between medial  
45 microvilli, which explains the restricted motion of protrusions in the marginal zone. Finally,  
46 long-term live imaging revealed that the accumulation of microvilli at cell margins  
47 consistently leads to accumulation in medial regions of the cell. Collectively, our findings  
48 suggest that nascent microvilli are stabilized by a capture mechanism that is localized to  
49 cell margins and enabled by the transjunctional formation of IMACs. These results inform  
50 our understanding of how apical specializations are assembled in diverse epithelial  
51 systems.

52

## 53 INTRODUCTION

54 Organ function depends on specialized cell types that have evolved morphologies to  
55 enable specific physiological tasks. Transporting epithelial cells, found in the intestine and  
56 kidney proximal tubule, offer interesting examples of this phenomenon. As important sites  
57 of solute uptake, maximizing apical surface area is a critical facet of these tissues. To  
58 meet this challenge, epithelial cells extend 1000s of bristle-like protrusions called  
59 microvilli, which pack tightly into a highly ordered array to collectively form a brush border  
60 [1, 2]. A single microvillus is a cylinder-shaped, micron-scale membrane protrusion  
61 supported by a core actin bundle consisting of 20-40 actin filaments [3, 4]. By scaffolding  
62 apical membrane in this way, microvilli amplify surface area available for solute transport  
63 and optimize solute uptake potential [5-7]. Microvilli first appear on the cell surface very  
64 early in epithelial maturation; differentiating cells, like those found within intestinal stem  
65 cell-containing crypts, exhibit few, poorly organized microvilli [8]. However, differentiated,  
66 fully functional enterocytes, found on the villus or within the kidney tubule, present a well-  
67 organized brush border consisting of densely packed protrusions [3, 9, 10].

68 Several previous studies established that tight microvillar packing is driven by a  
69 protocadherin-based intermicrovillar adhesion complex (IMAC), which physically links the  
70 distal tip of a microvillus to the tips of its neighboring microvilli [11-14]. In the case of the  
71 enterocyte, these adhesive interactions give rise to a hexagonal packing pattern when  
72 viewed *en face*, which represents maximum surface occupancy. Previous work also  
73 identified protocadherins CDHR2 and CDHR5 as the primary adhesive elements in these  
74 links, which form *trans* heterophilic adhesion complexes that are well suited for bridging  
75 the ~50 nm gap between neighboring microvilli [11, 15]. CDHR2 and CDHR5  
76 ectodomains contain multiple extracellular cadherin (EC) repeat motifs arranged in  
77 tandem, which are anchored to the membrane via a single spanning transmembrane  
78 domain [16]. Both protocadherins also contain cytoplasmic tails at their C-termini, which  
79 enable direct interactions with cytoplasmic IMAC binding partners including the actin-  
80 based motor, myosin-7B (MYO7B), and the scaffolding proteins, ankyrin repeat and  
81 sterile alpha motif domain containing 4B (ANKS4B) and usher syndrome 1C (USH1C)  
82 [12, 13, 17, 18]. Recently, calmodulin-like protein 4 (CALML4) was identified as a direct  
83 binding partner of MYO7B, making it an additional IMAC component [19]. KD studies of

84 MYO7B indicate that this motor plays a key role in the localization of CDHR2/CDHR5  
85 adhesion complexes to the distal tips of microvilli [12, 13]. In the differentiating CACO-  
86 2<sub>BBE</sub> intestinal epithelial cell culture model, disrupting the function of the IMAC via calcium  
87 chelators or knockdown of any single complex component leads to striking defects in  
88 microvillar growth and packing organization during differentiation [11-13, 19].  
89 Furthermore, complete loss of CDHR2 from intestinal and kidney epithelia in a villin-Cre  
90 driven knockout (KO) mouse, causes shortening and loss of brush border microvilli, a  
91 consequential decrease in the apical enrichment of key solute transporters, and reduced  
92 animal growth rate [14].

93 How new microvilli assemble and incorporate into a highly ordered brush border  
94 during differentiation remains unclear. Ultrastructural studies of native tissue and time-  
95 lapse imaging of epithelial cell culture models indicate that microvilli do not grow  
96 synchronously, but instead appear stochastically on the apical surface throughout  
97 differentiation [8, 11, 20]. One critical factor that promotes microvillar growth is the barbed  
98 end binder, epidermal growth factor receptor pathway substrate 8 (EPS8) [20, 21].  
99 Previous studies in multiple epithelial and non-epithelial systems have established that  
100 EPS8 is a highly specific marker of the distal ends of all forms of actin bundle supported  
101 protrusions [22-25]. Loss of this factor leads to shorter protrusions and increased length  
102 variability [26, 27]. Strikingly, on the apical surface of differentiating epithelial cells, EPS8  
103 arrives in diffraction-limited puncta at the membrane minutes before the subsequent  
104 growth of a core actin bundle and assembly of a microvillus at these sites [20]. Even once  
105 a core bundle begins to elongate, EPS8 puncta remain persistently associated with the  
106 distal end of the nascent structure. Following their initial growth, nascent microvilli are  
107 highly motile and translocate across the apical surface via a mechanism powered by  
108 treadmilling of the underlying core actin bundle [28], an activity that is also regulated by  
109 EPS8 [28]. Remarkably, if the distal tip of a newly formed microvillus loses its EPS8  
110 punctum, that structure rapidly collapses, suggesting that EPS8 serves as a microvillus  
111 survival factor [20]. These data also point to a previously unrecognized dynamic  
112 microvillus lifecycle, consisting of distinct phases of structural stability and instability. For  
113 microvilli to eventually accumulate in large numbers on the apical surface, this cycle must

114 ultimately tilt in favor of stability. However, how dynamic, nascent microvilli are stabilized  
115 on the apical surface so that they eventually accumulate long-term remains unknown.

116 Here we report our discovery of an adhesion-based mechanism that epithelial cells  
117 use to stabilize and in turn, drive the accumulation of microvilli during differentiation.  
118 Because microvillar growth takes place as differentiating enterocytes move through the  
119 crypt-villus transition [8], we reasoned that we could gain insight on mechanisms of  
120 microvilli accumulation by careful inspection of apical morphology in this region. Using  
121 this approach, we discovered that crypt microvilli initially accumulate at cell margins,  
122 implying the existence of a mechanism for anchoring nascent protrusions at these sites.  
123 We observed similar marginal accumulation of microvilli on the surface of differentiating  
124 intestinal and kidney epithelial cell lines. In all models examined, microvilli extending from  
125 one cell span intercellular space to make physical contact with microvilli on a neighboring  
126 cell. Using super-resolution microscopy, mechanistic studies in epithelial cell culture  
127 models, and live imaging, we determined that these points of physical contact represent  
128 “*transjunctional IMACs*” containing both CDHR2 and CDHR5, which are highly stable  
129 complexes that capture nascent microvilli and constrain their motion. Consistent with this  
130 point, long-term live imaging revealed that microvilli accumulation at cell margins  
131 outpaces accumulation in medial regions of the surface early in differentiation. Thus,  
132 microvilli extending from neighboring epithelial cells participate in a novel form of epithelial  
133 cell-cell contact that promotes apical surface maturation. The adhesion-based capture  
134 mechanism reported is likely to inform our understanding of apical morphogenesis in  
135 other epithelial cell types that build surface specializations.

136

## 137 RESULTS

### 138 Differentiating epithelial cells exhibit a marginal enrichment of microvilli

139 To begin to understand how microvilli are stabilized and accumulate in large numbers  
140 during differentiation, we first examined the distribution of nascent protrusions early in the  
141 maturation process. To this end, we used scanning electron microscopy (SEM) to survey  
142 the apical surface of the crypt cells in fractured samples of mouse small intestine. Within  
143 the crypt, where immature enterocytes are actively assembling a brush border (**Fig. 1A, zoom**), we noted a striking enrichment of microvilli at cell margins (**Fig. 1B, zoom 1 and**

145 **2 blue outlines**). In contrast, medial regions of the apical surface presented only a few,  
146 sparse microvilli (**Fig. 1B**). Thus, *in vivo*, microvilli appear to accumulate at the edges of  
147 cells during the early stages of brush border assembly.

148 To determine if the marginal accumulation of microvilli that we observed on the  
149 surface of differentiating crypt cells *in vivo* could be recapitulated *in vitro*, we first turned  
150 to the CACO-2<sub>BBE</sub> line. CACO-2<sub>BBE</sub> cells are a human intestinal epithelial cell culture  
151 model that builds a well-organized brush border over the course of several weeks at post-  
152 confluence [29]. SEM imaging of CACO-2<sub>BBE</sub> cells early in the differentiation time-course  
153 revealed a concentration of microvilli at cell margins similar to that observed in native  
154 crypts (**Fig 1C**). Moreover, protrusions in these regions appeared to span cell junctions  
155 and make physical contact with structures on neighboring cells (**Fig. 1C, zoom blue**  
156 **arrows**). As an additional point of comparison, we also examined SEM images of sub-  
157 confluent porcine kidney proximal tubule LLC-PK1 clone 4 (CL4) cells [30], which also  
158 exhibited a marginal accumulation of microvilli (**Fig. 1D, zoom blue outline**), even at the  
159 earliest stages of cell surface organization (i.e. subconfluence). Based on these *in vivo*  
160 and *in vitro* observations, the differentiating apical surface is characterized by two distinct  
161 populations of microvilli, marginal vs. medial (**Fig. 1E**), with the marginal region  
162 demonstrating higher protrusion packing density at these early time points.

163

#### 164 **Microvilli adopt a vertical orientation upon arriving at cell margins**

165 In the ultrastructural images alluded to above, we noted that marginal microvilli appeared  
166 more vertically oriented relative to microvilli extending from medial parts of the cell  
167 surface. Here we use ‘vertical’ to describe an orientation that is parallel to the long  
168 (apicobasal) axis of the cell and perpendicular to the plane of the apical surface. To  
169 confirm this observation under hydrated conditions, we performed volume imaging of live  
170 sub-confluent CL4 cells expressing mCherry-Espin (ESPN), which serves as a highly  
171 specific marker of microvillar core actin bundles [20, 28, 31, 32] (**Fig. 2A**). Lateral viewing  
172 of reconstructed volumes enabled us to visualize individual microvilli and obtain  
173 measurements of their orientation relative to the plane of the apical surface. This analysis  
174 revealed that the marginal and medial microvilli demonstrate significant differences in

175 their angle of protrusion, with marginal microvilli exhibiting a more vertical orientation  
176 ( $46.5^\circ \pm 19.3^\circ$  vs.  $77.3^\circ \pm 12.4^\circ$ , **Fig. 2B**).

177 Previous studies established that nascent microvilli are highly dynamic, growing,  
178 collapsing, and adopting a range of angles while undergoing active movement across the  
179 medial cell surface [20, 28]. With this in mind, we next sought to determine if microvilli  
180 grow in a vertical orientation at marginal sites or instead, grow medially and then adopt a  
181 vertical orientation upon arriving at the cell edge. To this end, we performed multi-hour  
182 time-lapse volume imaging to record microvillar motion and orientation in 3D. To help us  
183 interpret these complex datasets, we depth-coded volumes with a multi-color look-up  
184 table (LUT) so that image planes located further from the apical surface were rendered  
185 with warmer colors. While the dense accumulation of microvilli at cell margins impaired  
186 our ability to resolve individual growth events at these sites, we did observe individual  
187 protrusions and small adherent clusters of microvilli migrating while maintaining a small  
188 angle relative to the medial apical surface, as previously described [20, 28]. Following  
189 these microvilli over time (> 2 hrs) revealed that upon reaching the cell margin, they  
190 become more vertically orientated as indicated by the distal tips acquiring a warmer color  
191 coding (**Figs. 2C,D and Video S1**). Although these data do not allow us to rule out the  
192 possibility that microvilli grow *de novo* in a vertical orientation in the marginal zone, they  
193 do indicate that medial microvilli can transition into the marginal zone and adopt a vertical  
194 orientation upon doing so.

195

### 196 **Marginal microvilli are less motile than medial microvilli**

197 Vertically orientated microvilli are a defining feature of mature brush borders on the  
198 surface of villus enterocytes [3]. Based on this point, the vertically oriented microvilli found  
199 in the marginal zone may represent more mature, and potentially, more stable  
200 protrusions. To begin to test this concept, we expressed EGFP-EPS8 to specifically mark  
201 the distal tips of microvilli [20, 21] in CL4 cells also expressing mCherry-ESPN (**Fig. 3A,**  
202 **zooms**). We then performed live volume imaging with the goal of using the punctate and  
203 stoichiometric EPS8 signal (one punctum per microvillus) as a high-fidelity fiducial marker  
204 for tracking microvillar dynamics over time. Temporal color coding of the ESPN channel  
205 over the course of 25 minutes revealed that medial microvilli are highly dynamic and

206 demonstrate extensive movement as previously reported [28] (**Fig. 3B, zoom 1**). In  
207 contrast, marginal microvilli appeared to dwell for long periods near the edge of the cell,  
208 as indicated by the white band of color (merged colors of time points 0-25 min) in the  
209 projection (**Fig. 3B, zoom 2**). Next, we tracked individual EGFP-EPS8 puncta and  
210 generated rose plots of the resulting trajectories to examine the extent of motion  
211 demonstrated by individual microvilli. This analysis revealed that medial microvilli produce  
212 long trajectories consistent with directed motion, sampling an area of up to  $6 \mu\text{m}^2$  during  
213 the time-lapse period (**Figs. 3C,D**). By comparison, the trajectories of marginal microvilli  
214 were highly confined, with individual protrusions traveling less than  $2 \mu\text{m}^2$  over the same  
215 time course (**Figs. 3F,G**). Mean squared displacement analysis of trajectory data [28]  
216 confirmed that marginal microvilli are ~10-fold more constrained in their movement (**Fig.**  
217 **3H**) relative to medial protrusions (**Fig. 3E**). Together, these data suggest the existence  
218 of a mechanism for restricting the motion of microvilli at cell margins.  
219

## 220 **Microvilli from neighboring cells are linked by transjunctional adhesion complexes 221 containing CDHR2 and/or CDHR5**

222 Our ultrastructural data suggested that marginal accumulations of microvilli might include  
223 protrusions from both cells of a neighboring pair (**Fig. 1C zoom**). This led us to consider  
224 the possibility that microvilli extending from one cell may span the junctional space and  
225 physically contact microvilli from an adjacent cell; such interactions might in turn explain  
226 the upright orientation, reduced motility, and eventual accumulation of microvilli at these  
227 sites. One potential mechanism for mediating such interactions involves the  
228 intermicrovillar adhesion complex (IMAC), which includes the protocadherins CDHR2 and  
229 CDHR5 as core components [11]. Previous studies established that CDHR2 and CDHR5  
230 target to the distal tips of microvilli and interact with each other to form a  $\text{Ca}^{2+}$ -dependent  
231 heterophilic extracellular adhesion complex that spans the ~50 nm between adjacent  
232 protrusions [8-10]. The resulting link promotes the tight packing of neighboring microvilli  
233 and contributes to minimizing length variability throughout the larger structure of the brush  
234 border [16]. Notably, these previous studies on IMAC function focused solely on *medial*  
235 microvilli, so the possibility that this complex might also link microvilli from neighboring  
236 cells remains unexplored.

237 To test this idea, we used an immunostaining approach and super-resolution  
238 structured illumination microscopy (SIM) to examine the localization of CDHR2, CDHR5,  
239 and F-actin relative to ZO-1, a critical component of tight junctions [33]. For these studies,  
240 we first examined native small intestinal tissues isolated from a new mouse model  
241 expressing CDHR2 tagged with EGFP at the endogenous locus. SIM images revealed  
242 that both IMAC protocadherins are highly enriched at the tips of medial microvilli as  
243 previously reported (**Fig. 4A**) [11]. We also noted signal from CDHR2 and CDHR5 at the  
244 tips of microvilli at the margins of cells, with the adhesion protein signal spanning ZO-1  
245 marked junctions (**Fig. 4B, top panel**). When viewing projected SIM volumes *en face*, we  
246 were unable to discern the position of the tight junctions based solely on the phalloidin,  
247 CDHR2, or CDHR5 signals, suggesting that the IMAC components form a continuous  
248 network that spans beyond the surface of a single cell (**Fig. 4B, bottom panel**). Similarly,  
249 on the surface of mature enterocytes viewed with electron microscopy, microvilli appear  
250 to associate at neighboring cell interfaces (**Fig. S1A-B**). However, the crowded nature of  
251 microvilli in these mature brush borders confounded our attempts to isolate and visualize  
252 interactions between the tips of individual protrusions at the margins of neighboring cells.  
253

To work around the limitation imposed by microvillar crowding in native tissue, we  
254 used SIM to examine the apical surface of cultured CACO-2<sub>BBE</sub> cells at 12 days post-  
255 confluence (DPC), a time point *before* brush border assembly is complete, when  
256 microvillar packing density is comparatively lower. Careful examination of phalloidin-  
257 stained CACO-2<sub>BBE</sub> monolayers revealed a striking enrichment and alignment of microvilli  
258 at the margins of cells (**Fig. 4C,D**), consistent with the SEM images described above (**Fig.**  
259 **1B**). Immunofluorescence staining of these 12 DPC cultures revealed that marginally  
260 aligned microvilli do in fact span the cell junction marked by ZO-1 and exhibit enrichment  
261 of both protocadherins at their distal tips (**Fig. 4C,D, white arrows**). We observed similar  
262 structures and staining on the surface of CL4 monolayers at 3 DPC, a stage in  
263 differentiation when microvilli are still sparse but begin to form clusters and demonstrate  
264 marginal alignment (**Fig. 4E**). In this case, super-resolution lateral views clearly showed  
265 that individual microvilli from neighboring cells span the ZO-1-labeled tight junction and  
266 make contact via their distal tips, which are marked by both CDHR2 and CDHR5 (**Fig. 4F**

267 **zooms).** In combination, these results indicate that marginal microvilli on neighboring  
268 cells are physically linked via *transjunctional* IMACs that contain CDHR2 and CDHR5.  
269

270 **Heterophilic adhesion between CDHR2 and CDHR5 promotes robust association  
271 between microvilli from neighboring cells**

272 Although IMAC protocadherin adhesion properties differ across species [16], previous  
273 biochemical studies established that in humans, heterophilic complexes of CDHR2 and  
274 CDHR5 exhibit strong adhesion, CDHR2 demonstrates weak homophilic adhesion, and  
275 CDHR5 demonstrates no homophilic adhesion [11]. To further study the nature of  
276 transjunctional IMACs, we developed a cell mixing approach that enabled us to drive the  
277 formation of adhesion complexes consisting of different complements of CDHR2 and/or  
278 CDHR5 (**Fig. 5A**). For these experiments, we first transfected CL4 cells with either EGFP  
279 or mCherry-tagged constructs of *H. sapiens* CDHR2 and CDHR5. Stable selection and  
280 subsequent fluorescence-activated cell sorting (FACS) yielded robust populations of  
281 fluorescent protocadherin expressing cells (**Fig. S2A**). Strikingly, mixed monolayers  
282 composed of cells expressing CDHR2-EGFP or CDHR5-mCherry demonstrated robust  
283 alignment of protocadherin signals at mixed cell-cell contacts (**Fig. 5B**). Linescan analysis  
284 also revealed that CDHR2 and CDHR5 intensities were well correlated (mean  $r = 0.70$ )  
285 along these interfaces (**Fig. 5C,D,K**). These data are consistent with the formation of  
286 heterophilic adhesion complexes between microvilli of neighboring cells. In mixed  
287 monolayers composed of cells expressing CDHR2-EGFP or CDHR2-mCherry (**Fig. 5E**),  
288 mixed cell-cell contacts lacked the strong alignment of signals that we observed in the  
289 heterophilic case, and protocadherin intensities were poorly correlated (mean  $r = 0.07$ )  
290 (**Fig. 5F,G,K**). Mixed monolayers composed of cells expressing CDHR5-EGFP or  
291 CDHR5-mCherry also demonstrated a lack of signal alignment and poor intensity  
292 correlation along cellular junctions (mean  $r = -0.19$ ) (**Fig. 5H-K**). High-resolution imaging  
293 of the interfaces formed under each of these three conditions revealed that only  
294 heterophilic mixtures of cells expressing CDHR2-EGFP or CDHR5-mCherry aligned their  
295 microvilli at cell-cell contacts (**Fig. S2B-D, white arrows**). Based on these data, we  
296 conclude that heterophilic transjunctional IMACs containing CDHR2 and CDHR5 can  
297 drive robust interactions between microvilli extending from neighboring cell margins.

298 **Protocadherins in transjunctional IMACs exhibit limited turnover**

299 Under normal conditions, epithelial cells express both CDHR2 and CDHR5, which target  
300 to the tips of all microvilli on the apical surface. Thus, heterophilic complexes are expected  
301 to form between the distal tips of microvilli in both the medial and marginal regions.  
302 However, the strong alignment of microvilli at cell-cell contacts in the heterophilic case  
303 outlined above led us to predict that transjunctional IMACs may be more stable relative  
304 to complexes that form medially. If true, this would offer a mechanistic explanation for the  
305 reduced motility of marginal microvilli, and in turn, the accumulation of microvilli at these  
306 sites. To determine if transjunctional IMACs are in fact longer lived than medial  
307 complexes, we performed fluorescence recovery after photobleaching (FRAP) analysis  
308 with CL4 monolayers formed using the cell mixing approach outlined above (**Fig. 5A**).  
309 Strikingly, photobleached ROIs positioned over junctional interfaces between heterophilic  
310 CDHR2-EGFP and CDHR5-mCherry expressing cells demonstrated extremely low signal  
311 recovery for both protocadherins (immobile fractions, 0.71 and 0.85, respectively; **Figs.**  
312 **6A,B and Video S2**). In contrast, FRAP analysis of medially positioned ROIs on individual  
313 cells expressing both CDHR2-HALO and CDHR5-EGFP, revealed much lower immobile  
314 fractions for both protocadherins (0.47 and 0.56, respectively; **Figs. 6C,D and Video S3**).  
315 These results suggest that transjunctional IMACs formed between marginal microvilli are  
316 much longer lived relative to complexes formed between the tips of medial microvilli. We  
317 also examined recovery in photobleached ROIs positioned over junctional interfaces  
318 formed between homophilic CDHR2-EGFP and CDHR2-mCherry expressing cells (**Figs.**  
319 **6E,F and Video S4**), as well as interfaces formed between homophilic CDHR5-EGFP  
320 and CDHR5-mCherry expressing cells (**Figs. 6G,H and Video S5**). Both homophilic  
321 scenarios exhibited higher levels of turnover and even lower immobile fractions. Together,  
322 these FRAP studies indicate that transjunctional IMACs composed of CDHR2 and  
323 CDHR5 are extremely stable, and these reduced turnover kinetics offer a explanation for  
324 the constrained motility and accumulation of microvilli observed at cell margins.

325

326 **Microvillar packing density at cell margins is higher than the medial zone during**  
327 **differentiation**

328 Based on the stabilizing nature of transjunctional IMACs, we predicted that, during  
329 differentiation, cells might assemble the brush border by packing microvilli inward from  
330 cell margins. To test this idea, we performed extended time-lapse imaging of CL4 cells  
331 expressing mCherry-ESPN to stoichiometrically label microvillar core actin bundles (**Fig.**  
332 **7A-C**)<sup>[32]</sup>. Comparing regional ESPN intensities on a per cell basis, we found that  
333 marginal ESPN intensity increased almost ~2-fold more than medial signal during 24 hrs  
334 of differentiation (**Fig. 7D**). These timelapse results are consistent with the idea that  
335 microvilli accumulate first at cell margins and then pack inwards from the edges of the  
336 cell over time.

337

## 338 **DISCUSSION**

339 Previous live imaging studies of epithelial cells at times points early in differentiation  
340 established that actively growing and newly formed microvilli are highly motile and  
341 unstable, undergoing rapid cycles of growth and collapse [20, 28]. Those discoveries  
342 immediately led us to question how dynamic, nascent microvilli are stabilized long-term  
343 on the apical surface to enable their timely accumulation in large numbers (i.e.,  
344 thousands) by the end of differentiation. We first sought to approach this question by  
345 examining the surface of the undifferentiated epithelial cells that line the interior of the  
346 intestinal crypt, where microvillar growth activity is high. Because the apical surface of  
347 cells in this region is not yet fully packed with protrusions, we were hoping to identify  
348 patterns in the distribution of nascent microvilli that might offer insight on underlying  
349 mechanisms of stability.

350 Peering into the crypt is technically challenging given the tight confines of this  
351 invaginated compartment. Indeed, almost all previous ultrastructural studies of this region  
352 have been limited to conventional transmission EM of ultrathin sections [34, 35], which  
353 are difficult to interpret in the absence of 3D context. We worked around this obstacle  
354 using a combination of tissue fracturing and scanning EM, which allowed us to visualize  
355 the apical surface of immature intestinal epithelial cells within the crypt. Inspection of  
356 these images revealed that microvilli preferentially accumulate near the cell periphery at  
357 this point in differentiation. Moreover, cell culture models from the intestine (CACO-2<sub>BBE</sub>)  
358 and kidney (CL4) also demonstrated robust marginal accumulation of microvilli early in

359 their maturation time course, suggesting that such patterning is not a function of the  
360 unique cellular packing geometry found in the crypt, nor is it tissue specific.

361        Accumulation of microvilli at cell edges suggests that the marginal zone represents  
362 (i) a site of robust growth, (ii) a site of stabilization for nascent microvilli, or (iii) some  
363 combination of the two. Given the actin-rich junctional belt that surrounds the cell at the  
364 level of the terminal web [36], it seems reasonable to expect that microvilli may grow more  
365 readily in this location. Although previous live imaging studies of CL4 cells characterized  
366 the properties of individual microvillar growth events [20], those observations were limited  
367 to the medial regions of the cell where protrusion density is typically low; visualization of  
368 growth events in the marginal zone was confounded by the crowding of pre-existing  
369 microvilli in this region. While our data do not allow us to rule out the possibility that growth  
370 preferentially occurs at cell margins relative to medial regions, we were able to capture  
371 clear examples of clustered microvilli moving at a low angle relative to the cell surface,  
372 toward the edge of the cell and incorporating into the marginal population. Interestingly,  
373 these protrusions adopt the more vertical orientation of marginal microvilli upon reaching  
374 the cell edge. Because such upright orientation is a defining feature of microvilli in mature  
375 brush borders, the marginal population likely represents stabilized protrusions that persist  
376 into later stages of differentiation. Although we currently lack a method for tracking and  
377 measuring the lifetimes of individual microvilli over the course of days, our short-term  
378 tracking measurements using the tip marker, EPS8, confirm that marginal microvilli are  
379 less motile relative to medial microvilli. Indeed, using mean square displacement analysis  
380 as previously described [28], we found that marginal microvilli sample ~10-fold less  
381 surface area per unit time relative to medial microvilli, which is consistent with a physical  
382 capture mechanism near the cell edge.

383        Earlier work established that medial microvilli on the surface of mature villus  
384 enterocytes employ the protocadherins CDHR2 and CDHR5 to form intermicrovillar  
385 adhesion complexes (IMACs) that link the distal tips of neighboring microvilli [11, 15].  
386 Here we sought to test the possibility that IMACs form across cell junctions, between the  
387 protrusions that extend from neighboring cells. If so, this would offer a mechanistic  
388 explanation for the upright orientation and constrained motility that microvilli demonstrate  
389 at these sites, and potentially the long-term stabilization that enables microvillar

390 accumulation on the apical surface in large numbers. Previous work in CACO-2<sub>BBE</sub> cells,  
391 native mouse intestinal tissue, and X-ray crystallography all indicate that the interacting  
392 ectodomains of CDHR2 and CDHR5 are structurally capable of spanning gaps up to 63  
393 nm wide [11, 16], suggesting that they could easily reach across the ~15 nm tight junction  
394 between neighboring cells [37]. Indeed, in the current study, super-resolution imaging  
395 revealed that CDHR2 and CDHR5 span the intercellular space to form *transjunctional*  
396 IMACs that physically link marginal microvilli that extend from neighboring cells.

397 Does the formation of transjunctional IMACs explain the accumulation of microvilli  
398 at cell edges early in differentiation? If transjunctional IMACs are more stable and exhibit  
399 longer lifetimes relative to IMACs that form medially, this would certainly offer a  
400 mechanistic underpinning for the increase in microvilli density at these sites. To test this  
401 hypothesis, we employed a cell mixing approach that enabled us to induce the formation  
402 of both homophilic and heterophilic transjunctional IMACs, to enable further  
403 characterization of their properties. FRAP analysis of the turnover dynamics of these  
404 complexes revealed that heterophilic (CDHR2/CDHR5) transjunctional IMACs are much  
405 longer lived relative to homophilic (CDHR2/CDHR2) complexes. These results from live  
406 epithelial cells echo previous *in vitro* data suggesting that homophilic (CDHR2/CDHR2)  
407 complexes are much weaker than heterophilic (CDHR2/CDHR5) complexes [11].  
408 Interestingly, when we examined the dynamics of heterophilic complexes formed between  
409 microvilli in the medial population, we noted that these also turned over at a much higher  
410 rate relative to transjunctional heterophilic (CDHR2/CDHR5) complexes. Thus, the  
411 significant differential stability of transjunctional vs. medial IMACs indicated by our FRAP  
412 studies offers a mechanistic rationale for the accumulation of microvilli at cell margins.

413 Why transjunctional IMACs are more stable than those formed elsewhere on the  
414 apical surface remains unclear, but possible explanations might be found in previous  
415 biophysical studies on the properties of non-covalent bonds. For example, when a tensile  
416 mechanical force is applied across a non-covalent bond formed between two proteins,  
417 the lifetime of that bond will be impacted in a way that depends on the structural nature  
418 of the bonding interface [38, 39]. “Slip bonds” react to loading with a dramatic shortening  
419 of lifetime, whereas “catch bonds” respond by increasing bond lifetime; “ideal bonds”  
420 exhibit minimal response to mechanical loading [38, 40, 41]. Direct physical

421 measurements provide strong evidence for catch bond behavior in structurally diverse  
422 proteins, ranging from myosin motor domains to cell surface molecules such as integrins  
423 [42, 43]. Cadherins have been studied extensively in this regard and their bonding  
424 properties are complex. In the case of E-cadherin, adhesive interactions can exhibit slip  
425 or catch behavior depending on the conformation of the adhesive interface. In the  
426 canonical strand swapped conformation, E-cadherin exhibits slip bond behavior; while X-  
427 dimers of E-cadherin, which interact using a distinct extended structural interface  
428 demonstrate robust catch bond behavior [40]. In light of those findings, we speculate that  
429 IMACs also exhibit catch bond properties. By bridging across cell junctions,  
430 transjunctional IMACs may be subject to higher tensile loads and therefore exhibit  
431 increased adhesive lifetimes relative to IMACs that form elsewhere on the apical surface.  
432 Furthermore, as medial clusters of microvilli appear to move as a unit [28], their adhesive  
433 bonds may be under less tensile stress. Although rigorous testing of this concept must  
434 await future biophysical studies, it is important to note that, based on the recently solved  
435 structures of mouse and human CDHR2 and CDHR5 ectodomains [16], any catch bond  
436 behavior in the IMAC would emerge from a mechanism that is distinct from E-cadherin.

437 Given the adhesive capture of microvilli by stable transjunctional IMACs and our  
438 observations of marginal microvilli enrichment early on in cell surface differentiation, we  
439 speculated that the brush border assembly may favor packing from the margins of the  
440 apical surface, inwards (**Fig. 7E**). To test this idea, we turned to multi-day time-lapse  
441 imaging of CL4 cells expressing mCherry-ESPN as a marker for microvilli. As expected,  
442 we noted that the marginal ESPN intensity was initially higher than in the medial region.  
443 After 24 hours of differentiation, the marginal region also demonstrated ~2-fold larger  
444 increase in signal relative to the medial zone, suggesting that microvillar packing density  
445 at the cell margin precedes packing of the interior apical surface. Moreover, intensity at  
446 the cell margin is consistently higher than medial signal, and both regions increase in  
447 intensity over the course of almost two days of observation. In future studies, it will be  
448 critical to confirm this observation in systems that more closely recapitulate the biology of  
449 the crypt-villus transition, such as intestinal organoids.

450 While previous work established that the IMAC is critical for maintaining brush  
451 border structure on mature enterocytes [14], the current study indicates a new role for this

452 complex in apical surface maturation, by contributing to a novel form of cell-cell contact  
453 between microvilli of neighboring cells. In the intestinal tract and other transporting  
454 epithelial tissue, cell-cell contacts are essential for “barrier” function and the maintenance  
455 of physical compartmentalization. Interestingly, Crohn’s Disease patients exhibit a  
456 decrease in CDHR2 and CDHR5 mRNA expression [44] while also experiencing  
457 increased intestinal permeability [45]. Transjunctional adhesion complexes may also form  
458 an additional layer of protection against colonizing pathogens. Infection by related  
459 pathogens Enteropathogenic and Enterohemorrhagic *Escherichia coli* (EPEC and EHEC)  
460 is characterized by effacement of brush border microvilli and F-actin pedestal formation  
461 [46]. CDHR2 has been identified as one of the initial EHEC targets during infection, which  
462 results in a significant decrease in CDHR2 expression [47]. Past reports on EPEC  
463 infection also show both bacteria localization over cell junctions [46, 48]. In the future  
464 studies, it will be fascinating to explore new roles for transjunctional IMACs in maintaining  
465 epithelial barrier function in intestinal disease and infection.

466

467 **ACKNOWLEDGMENTS**

468 The authors would like to thank all members of the M.J.T. laboratory for their constructive  
469 feedback. Special thanks goes to laboratory manager Suli Mao, for her work with mouse  
470 husbandry and genotyping. We acknowledge the Translational Pathology Shared  
471 Resource (NCI Cancer Center Support Grant 5P30CA68485-19) and also thank the  
472 Vanderbilt Genome Editing Resource (RRID: SCR\_018826). Microscopy was performed  
473 in part through the VUMC Cell Imaging Shared Resource. Some SEM images were  
474 collected on a Zeiss Crossbeam funded by 1S10 OD028704. Flow Cytometry  
475 experiments were performed in the VUMC Flow Cytometry Shared Resource supported  
476 by the Vanderbilt Ingram Cancer Center (P30 CA68485) and the Vanderbilt Digestive  
477 Disease Research Center (DK058404). This work was supported by the NIH grants  
478 DK095811, DK125546, DK111949 (M.J.T.) and the Training Program in Developmental  
479 Biology 2T32HD007502-20 (C.S.C.)

480

481 **AUTHOR CONTRIBUTIONS**

482 Conceptualization, C.S.C. and M.J.T.; Methodology, M.J.T., C.S.C., B.A.M. and E.S.K.;  
483 Validation, C.S.C.; Formal Analysis, C.S.C., J.B.S., and M.J.T.; Investigation, C.S.C.,  
484 J.B.S., L.M.M., and B.A.M.; Writing, C.S.C. and M.J.T.; Visualization, C.S.C.; Supervision,  
485 M.J.T.; Project Administration, M.J.T.; Funding Acquisition, C.S.C. and M.J.T.; All authors  
486 contributed to revising the manuscript.

487

488 **DECLARATION OF INTERESTS**

489 The authors declare no competing interests.

490

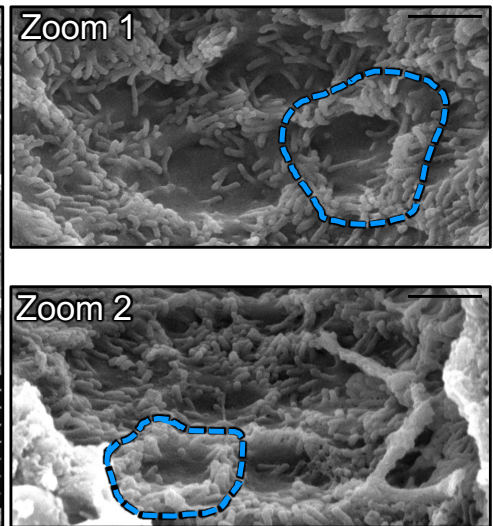
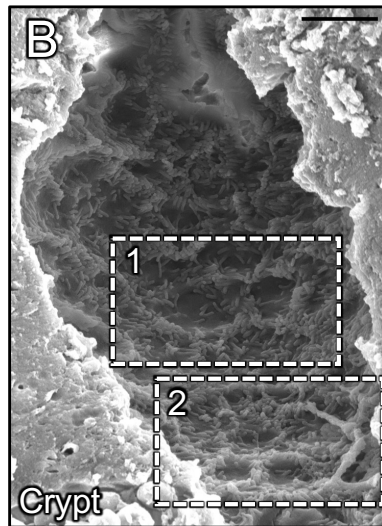
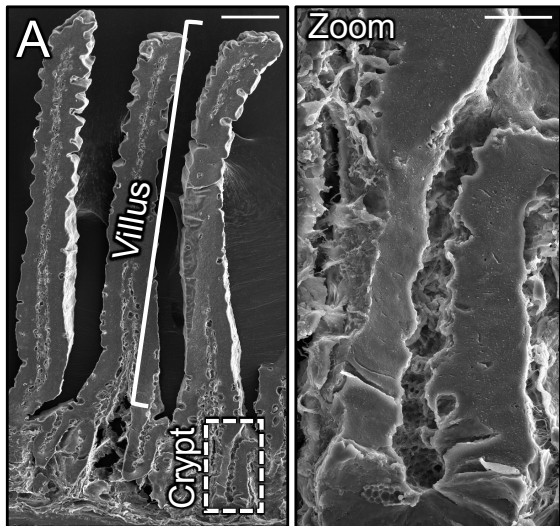
491 **INCLUSION AND DIVERSITY**

492 We support inclusive, diverse, and equitable conduct of research.

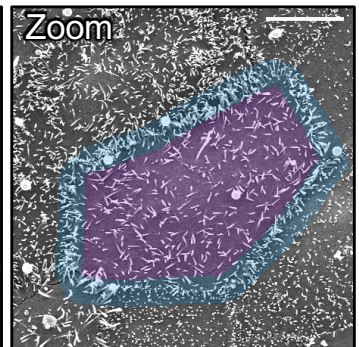
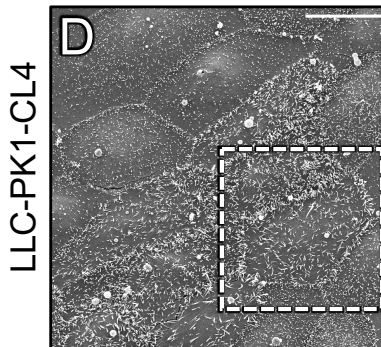
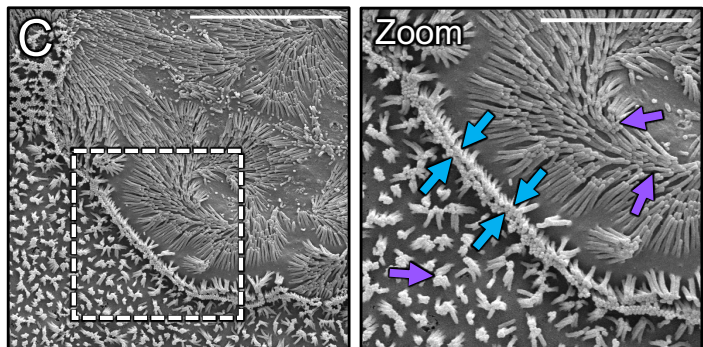
493

# Fig. 1

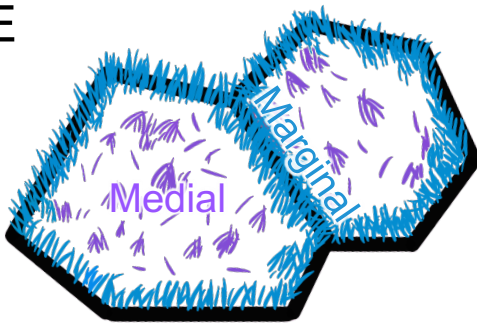
Mouse Small Intestine



CACO-2<sub>BBE</sub>



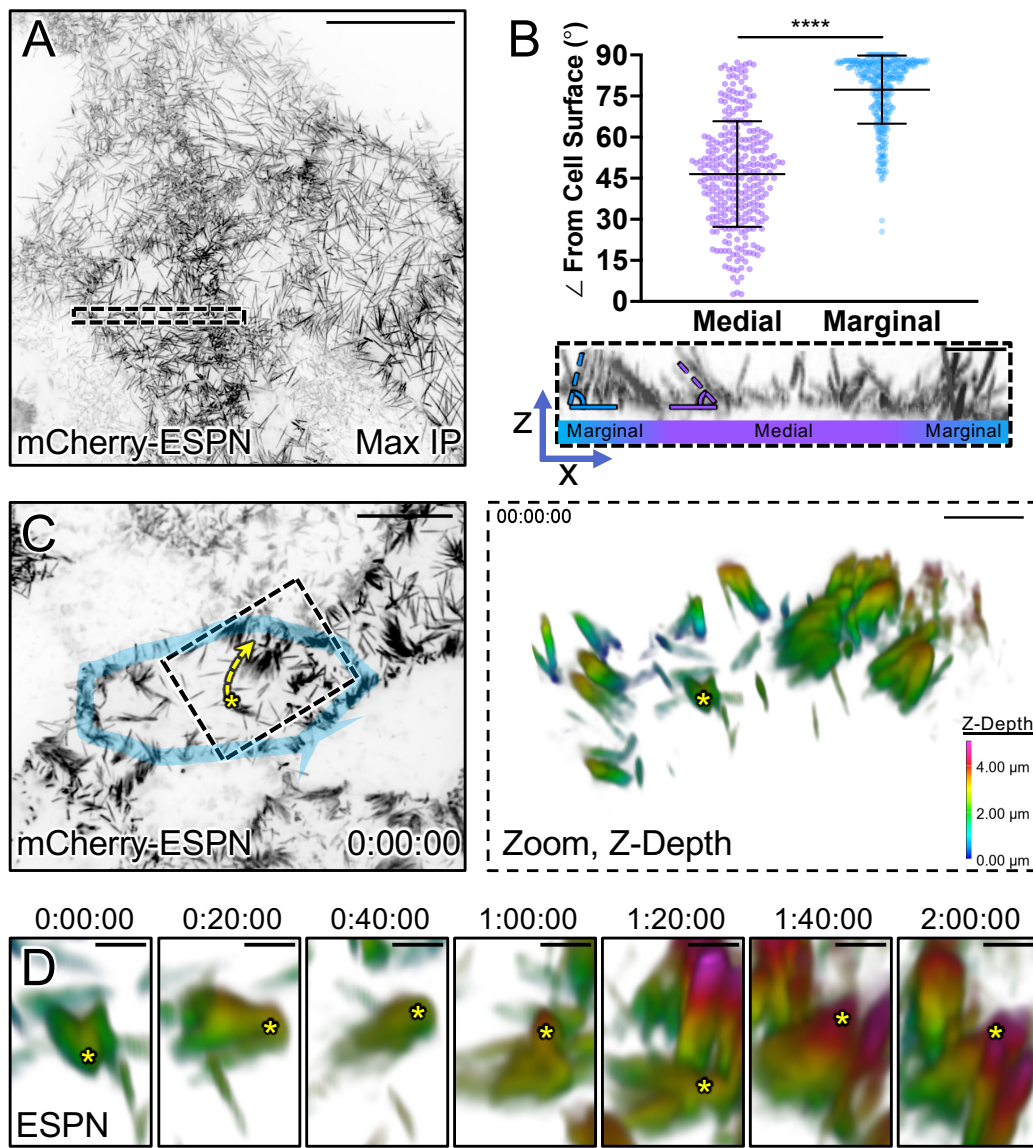
E



494 **Figure 1: Microvilli of differentiating transporting epithelial cells concentrate at cell**  
495 **margins.** **(A)** Scanning electron micrograph (SEM) of native mouse small intestine crypt-  
496 villus axis. **(A, zoom)** Zoom of the dashed box in A showing the crypt and transit  
497 amplifying zone. **(B)** High-magnification view of the crypt base with **(B, zooms 1 and 2)**  
498 showing an enrichment of microvilli at the margins of crypt cells (dashed blue outline). **(C)**  
499 SEM of polarized CACO-2<sub>BBE</sub> cells. Dashed box represents zoom area. Arrows denote  
500 medial (purple) and marginal microvilli (blue). **(D)** SEM of sub-confluent porcine kidney  
501 proximal tubule LLC-PK1-CL4 (CL4) cells. Dashed box represents zoom area. Pseudo  
502 coloring represents medial area (purple) and marginal microvillar area (blue). **(E)**  
503 Schematic of the two distinct organizations of microvilli found on differentiating  
504 transporting epithelial cells, medial (purple) and marginal (blue). Scale bars: 50 µm (A),  
505 10 µm (A, zoom), 2 µm (B), 1 µm (B, zooms), 10 µm (C), 5 µm (C, zoom), 20 µm (D), 10  
506 µm (D, zoom).

507

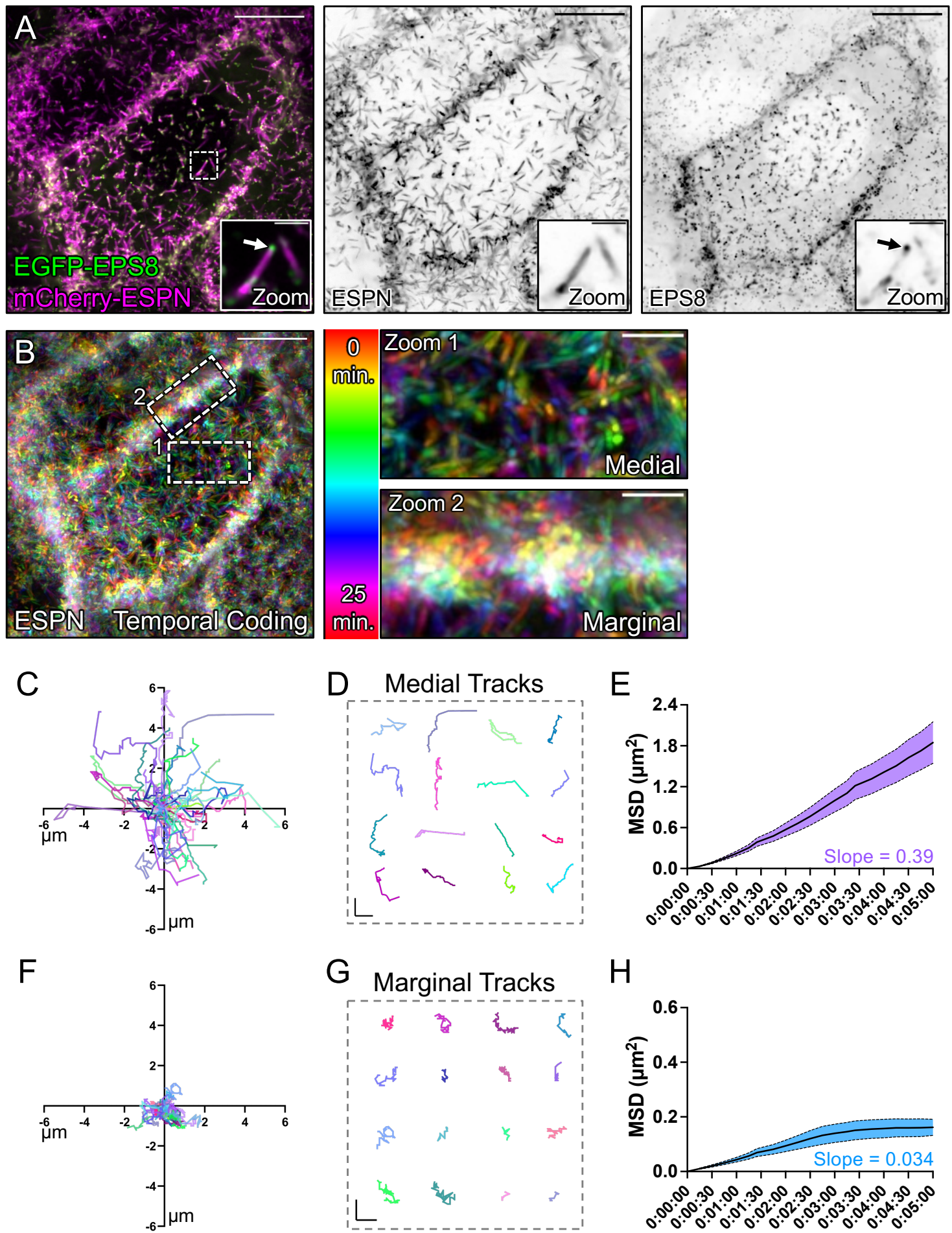
# Fig. 2



508 **Figure 2: Microvilli adopt a vertical orientation upon reaching cell margins. (A)**  
509 Maximum intensity projection (MaxIP) of live CL4 cells expressing mCherry-ESPN. **(B)**  
510 Orientation measurements of the angle (dashed outlines) of microvilli to the cell surface  
511 of medial microvilli (purple) compared to marginal microvilli (blue). Sample ROI of Z-  
512 projection under plot is taken from the dashed box in (A). **(C)** t = 0 MaxIP image of live  
513 mCherry-ESPN CL4 cells. One cell margin is highlighted in blue, while the dashed yellow  
514 arrow represents the trajectory of the microvilli cluster (asterisk) shown in (D). Right panel  
515 shows a 3D tilted volume of the dashed box in (C), coded in Z for cell depth (see Z-depth  
516 key on bottom right). **(D)** Montage over 2 hours following the cluster marked with the  
517 yellow asterisk in (C). Asterisk marks the distal ends of microvilli that transition to a vertical  
518 orientation upon reaching the marginal cell area, as shown by a change in Z-depth coding.  
519 Each point on the graph represents one angle taken from 17 cells; total of  $n = 295$  medial  
520 and  $n = 309$  marginal angles. Error bars represent mean  $\pm$  SD. \*\*\*\* p  $\leq 0.0001$  Welch's  
521 unpaired t-test. Mean medial angle is  $46.5^\circ \pm 19.3^\circ$  and mean marginal angle is  $77.3^\circ \pm$   
522  $12.4^\circ$ . Scale bars: 20  $\mu\text{m}$  (A), 1  $\mu\text{m}$  (B), 10  $\mu\text{m}$  (C, left), 3  $\mu\text{m}$  (C, right), 1  $\mu\text{m}$  (D).

523

# Fig. 3

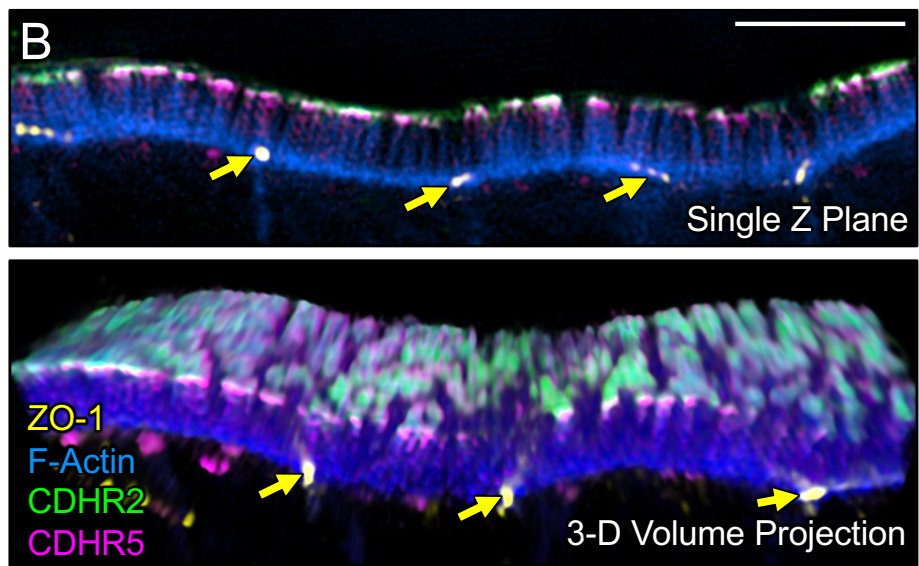
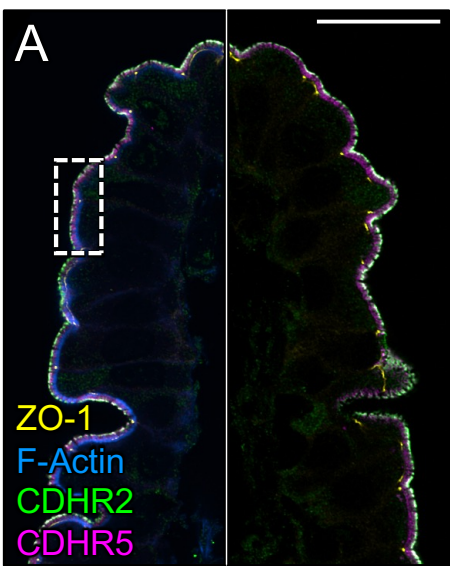


524 **Figure 3: Tip tracking analysis reveals that marginal microvilli are constrained in**  
525 **their movement. (A, left panel)** Live CL4 cells co-expressing EGFP-EPS8 and mCherry-  
526 ESPN. Dashed box represents zoom area with arrow marking EPS8 at the tip of a single  
527 microvillus. **(A, right panels)** Single inverted channel MaxIP images showing mCherry-  
528 ESPN and EGFP-EPS8 alone. **(B)** Temporal color-coding over 25 minutes (see vertical  
529 color key). **(B, zooms)** of **(1)** medial and **(2)** marginal ROIs taken from the dashed boxes  
530 in **(B)**. **(C)** Rose plot of  $n = 53$  XY tracks ( $\mu\text{m}$  units) of medial microvilli over 25 minutes.  
531 **(D)** Representative medial microvilli tracks taken from **(C)**. **(E)** Mean square displacement  
532 of 50 medial microvilli imaged for 5 minutes over 15 second intervals. Slope = 0.39. **(F)**  
533 Rose plot of  $n = 28$  XY tracks of marginal microvilli taken from 3 independent live cell  
534 imaging experiments over 25 minutes. **(G)** Representative marginal microvilli tracks taken  
535 from **(F)**. **(H)** Mean square displacement analysis of  $n = 88$  marginal microvilli imaged for  
536 5 minutes over 15 second intervals. Slope = 0.034. Scale bars: 10  $\mu\text{m}$  (A), 1.5  $\mu\text{m}$  (A,  
537 zooms), 10  $\mu\text{m}$  (B), 2.5  $\mu\text{m}$  (B, zooms), 1  $\mu\text{m}$  (D, G).

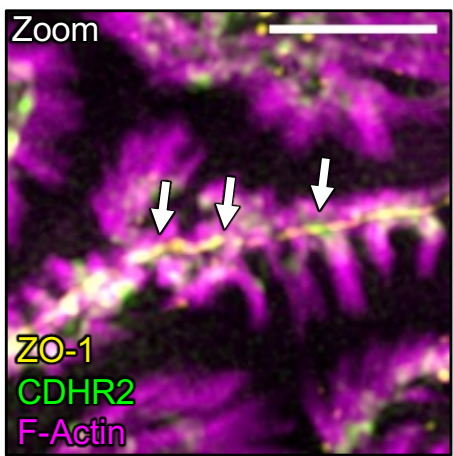
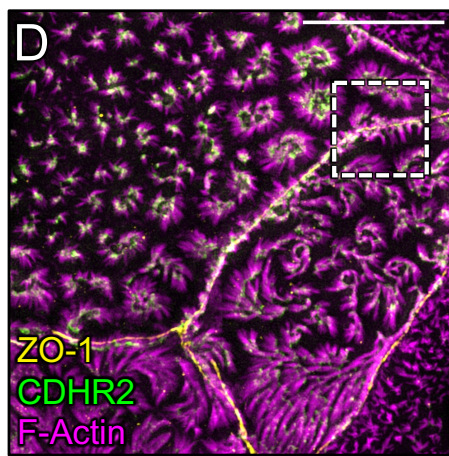
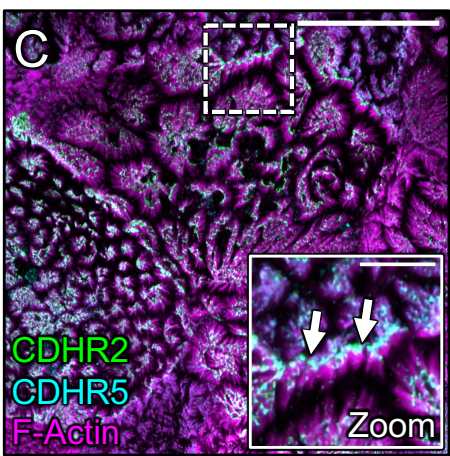
538

**Fig. 4**

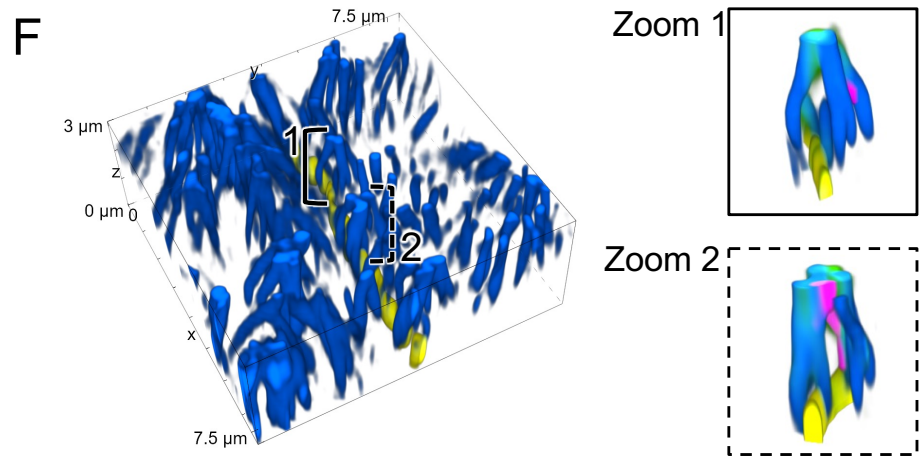
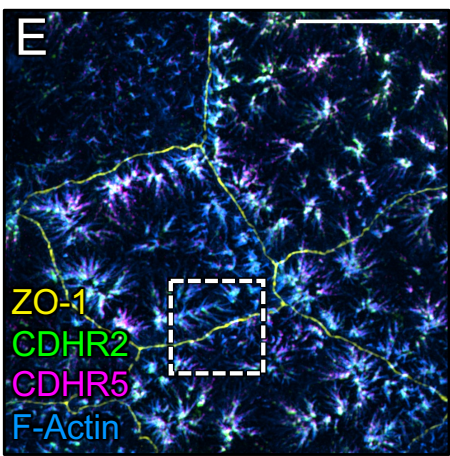
EGFP-CDHR2 Mouse SI



12DPC CACO-2<sub>BBE</sub>



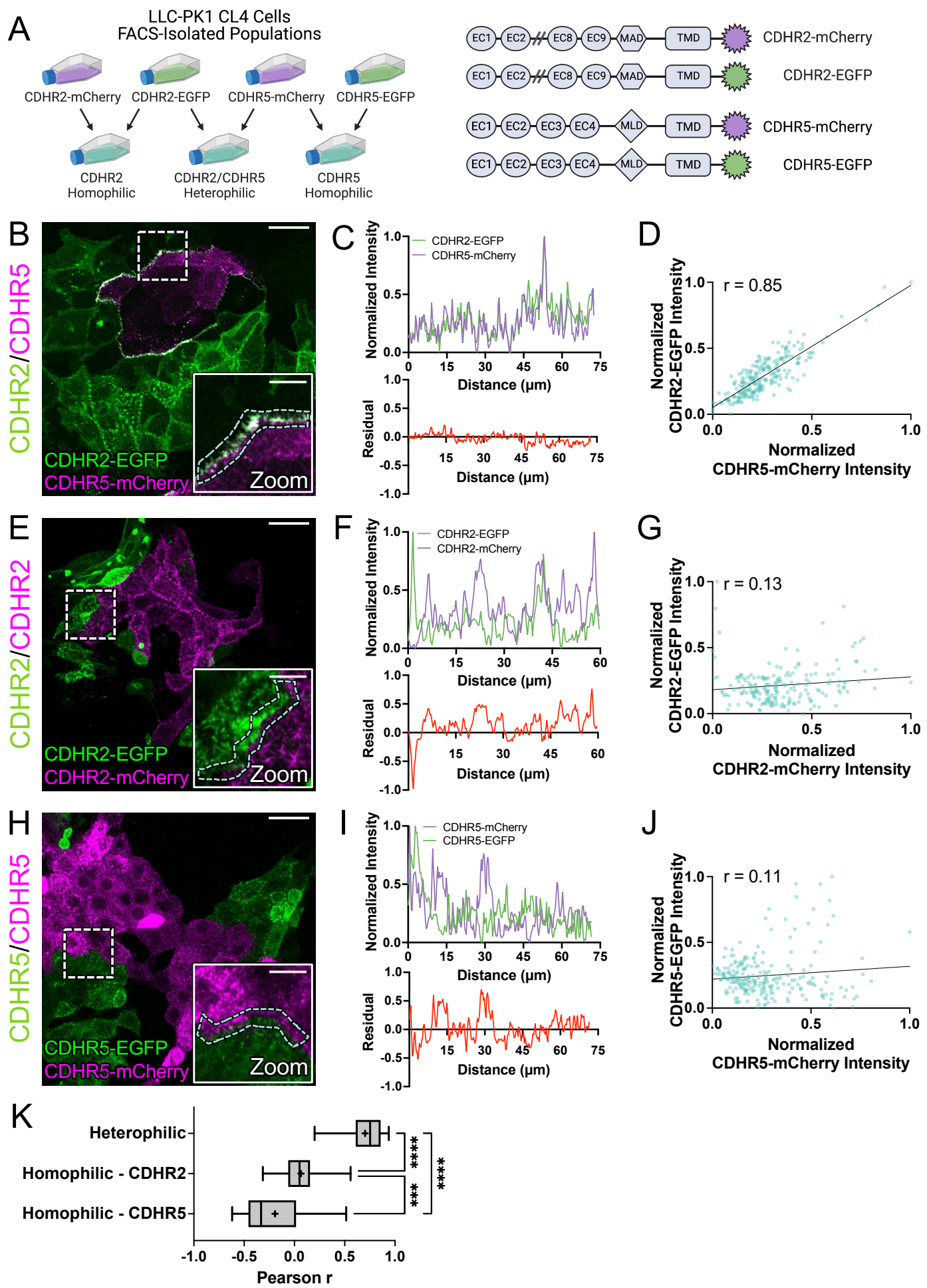
3DPC LLC-PK1-CL4



539 **Figure 4: Marginal microvilli are linked via transjunctional CDHR2/CDHR5 adhesion**  
540 **complexes across neighboring cell junctions.** **(A)** Single Z-plane confocal image of  
541 CDHR2-EGFP mouse small intestine stained for ZO-1 (yellow), EGFP (green), CDHR5  
542 (magenta), and F-actin (blue). **(B, top)** Single plane SIM image of the stained villus  
543 section; approximated area marked by the dashed box in (A). **(B, bottom)** 3D volume  
544 projection of the top panel. Yellow arrows in both images mark ZO-1 labeled tight  
545 junctions. **(C)** MaxIP laser-scanning confocal image of 12 DPC CACO-2<sub>BBE</sub> cells stained  
546 for CDHR2 (green), CDHR5 (cyan), and F-actin (magenta). Dashed box represents zoom  
547 area. White arrows point to tip-localized CDHR2/CDHR5 adhesion complexes at cell  
548 margins. **(D)** MaxIP SIM image of 12DPC CACO-2<sub>BBE</sub> cells stained for ZO-1 (yellow),  
549 CDHR2 (green), and F-actin (magenta). Dashed box represents zoom area. White arrows  
550 point to CDHR2/CDHR5 marked complexes at the junction of neighboring cells. **(E)** MaxIP  
551 SIM image of 3 DPC CL4 cells stained for ZO-1 (yellow), CDHR2 (green), CDHR5  
552 (magenta), and F-actin (blue). **(F)** 3D tilted volume projection of the dashed box outlined  
553 in (E). Brackets highlight instances of marginal microvilli on adjacent cells linked via  
554 CDHR2/CDHR5 transjunctional adhesion complexes (**zoom 1 and 2**, respectively). Scale  
555 bars: 20 µm (A), 5 µm (B), 2.5 µm (C), 5 µm (C, zoom), 10 µm (D), 2.5 µm (D, zoom), 10  
556 µm (E).

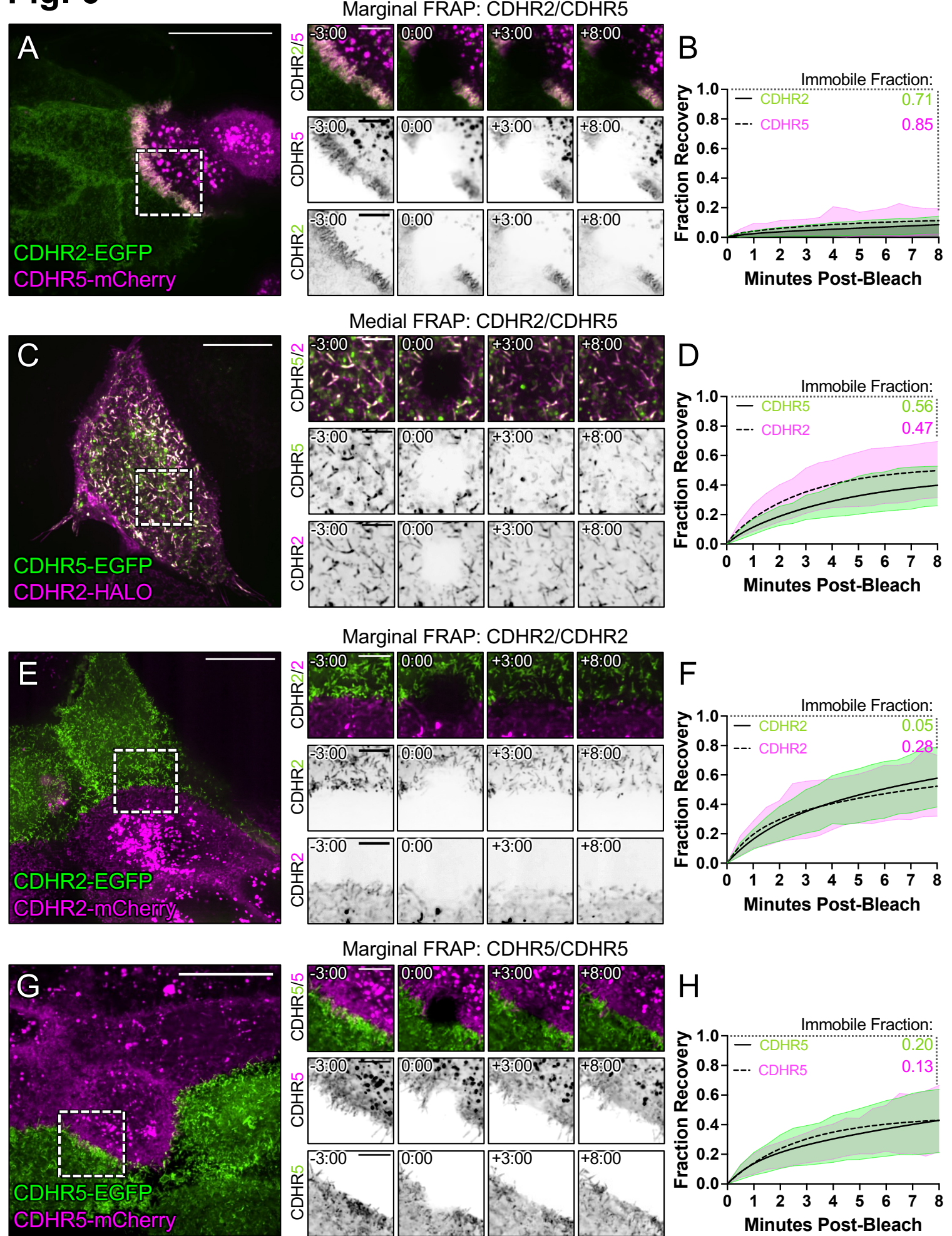
557

**Fig. 5**



558 **Figure 5: Cell mixing experiments reveal robust heterophilic adhesion complexes**  
559 **between marginal microvilli. (A, left)** Schematic depicting cell mixing method for the C-  
560 terminally tagged cadherin overexpression constructs **(A, right)**. **(B)** MaxIP laser  
561 scanning confocal image of mixed heterophilic CDHR2-EGFP and CDHR5-mCherry CL4  
562 cell populations. Dashed box represents zoom area and cyan dashed outline represents  
563 sample linescan. **(C, top)** Normalized fluorescence intensity (AU) plot taken from a  
564 representative linescan along the mixed cell interface. **(C, bottom)** Plotted difference  
565 (residual) of mCherry signal from EGFP signal from the top linescan plot. **(D)** Pearson's r  
566 correlation plot from the linescan in (C);  $r = 0.85$ . **(E)** MaxIP of mixed homophilic CDHR2-  
567 EGFP and CDHR2-mCherry CL4 cells. **(F-G)** Representative linescan and respective  
568 Pearson's r correlation;  $r = 0.13$ . **(H)** MaxIP of mixed homophilic CDHR5-EGFP and  
569 CDHR5-mCherry CL4 cells. **(I-J)** Representative linescan and respective Pearson's r  
570 correlation;  $r = 0.11$ . **(K)** Combined Pearson's r values from  $n = 30$  individual linescans of  
571 each cell mixing scenario from 3 independent fixation and staining experiments (10  
572 linescans per experiment). Mean Pearson's r values are denoted by a "+" for each  
573 scenario where heterophilic  $r = 0.703$ , homophilic CDHR2  $r = 0.065$ , and homophilic  
574 CDHR5  $r = -0.193$ . Ordinary one-way ANOVA with multiple comparisons; \*\*\*\*  $p \leq 0.0001$   
575 and \*\*\*  $p \leq 0.001$ . Scale bars: 30  $\mu\text{m}$  (B, E, H), 10  $\mu\text{m}$  (zoom insets).

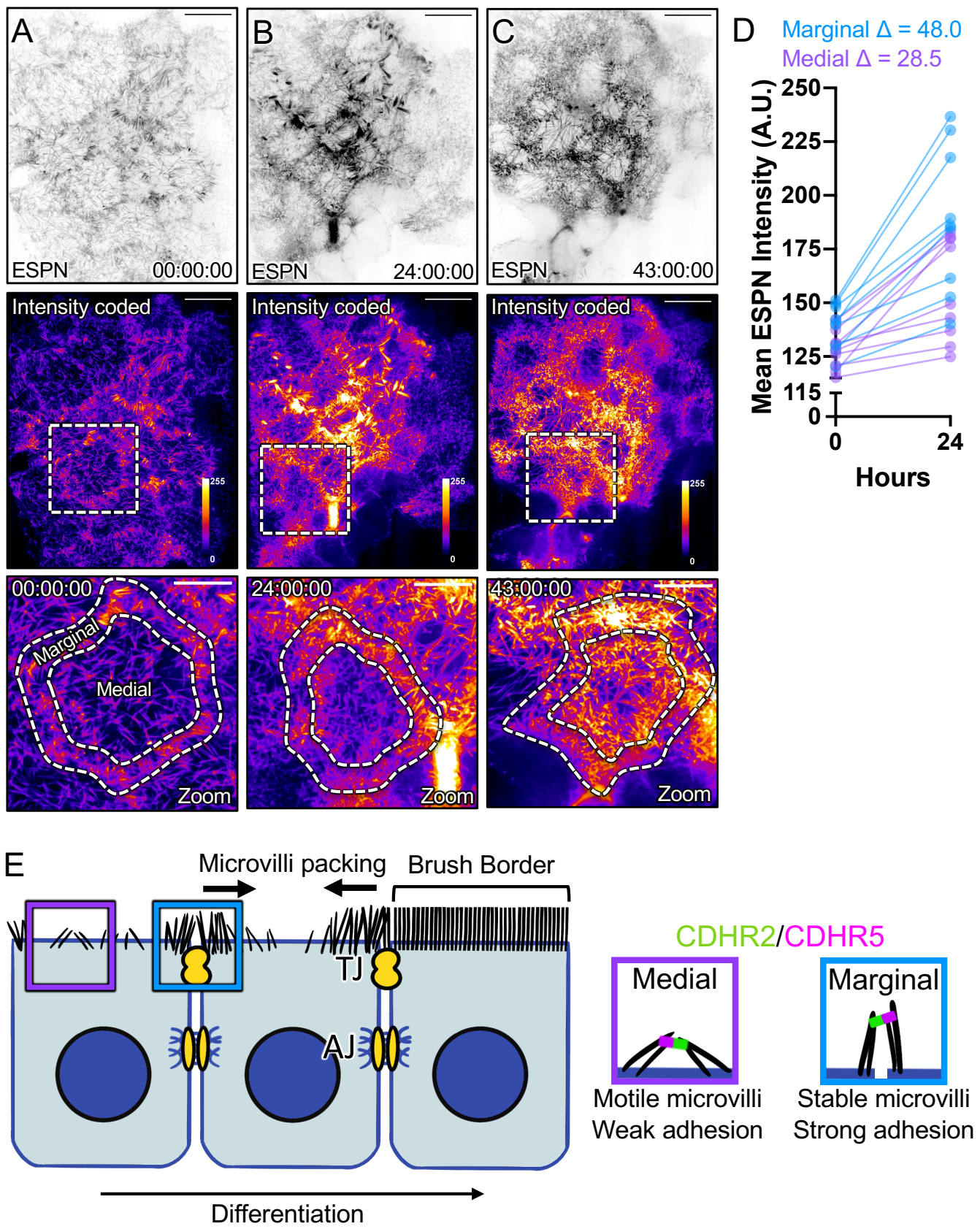
576

**Fig. 6**

577 **Figure 6: FRAP analysis suggests that heterophilic, transjunctional adhesion**  
578 **complexes are stable.** Mixed CL4 cells forming (**A**) marginal heterophilic, (**C**) medial  
579 heterophilic, (**E**) marginal homophilic CDHR2, and (**G**) marginal homophilic CDHR5  
580 adhesion complex interfaces. Dashed boxes outline the photobleached ROI shown in the  
581 recovery montages on right. (**B, D, F, H**) Fluorescence recovery is plotted over the course  
582 of 8 minutes with the immobile fractions as written for each protein channel. All plots  
583 represent 3 independent FRAP experiments of  $n \geq 20$  ROIs from multiple cells. Scale  
584 bars: 20  $\mu\text{m}$  (A, C, E, G), 5  $\mu\text{m}$  (montages).

585

# Fig. 7



586 **Figure 7: Long-term imaging reveals that microvilli first accumulate at cell margins**  
587 **over the course of differentiation.** (A-C) MaxIP spinning disk confocal stills of live  
588 mCherry-ESPN expressing CL4 cells at t = 0 hours, 24 hours, and 43 hours from a 43-  
589 hour acquisition. (A-C, intensity coded) Fire LUT intensity profile of the mCherry-ESPN  
590 channel. Intensity scales from low (0; dark purple) to high (255; yellow/white) as denoted  
591 by LUT profile. Zooms at each time point are outlined by dashed boxes, with marginal  
592 and medial zones as marked. (D) Mean marginal and medial mCherry-ESPN intensity of  
593  $n = 10$  cells from the time points shown in (A-C). Change in mean ESPN intensity (AU) in  
594 the first 24 hours is denoted on the graph. The cut axis accounts for background mCherry  
595 signal. Scale bars: 20  $\mu\text{m}$  (A-C), 10  $\mu\text{m}$  (zooms). (E) An adhesion-based model for the  
596 marginal stabilization of microvilli during brush border assembly. Microvilli on nascent  
597 transporting epithelial cells organize into two distinct populations: medial and marginal.  
598 Medial microvilli are highly motile while marginal microvilli are stable and stand at an  
599 orientation more vertical to the apical surface. Transjunctional CDHR2/CDHR5  
600 heterophilic adhesion complexes span cell-cell junctions and link marginal microvilli of  
601 neighboring cells. These complexes are long-lived, and lead to the accumulation of  
602 microvilli at the edges of cells. A predicted outside-in packing mechanism occurs during  
603 differentiation as a result of transjunctional adhesion complexes first stabilizing microvilli  
604 at cell margins.

605

606 **METHODS:**607 **Key Resources Table**

REAGENT or RESOURCE	SOURCE	IDENTIFIER
<b>Antibodies</b>		
anti-PCLKC [CDHR2] (mouse) [1:25]	Abnova	Cat# H00054825-M01; RRID: <a href="#">AB_490042</a>
anti-CDHR5 (rabbit) [1:250]	Sigma-Aldrich	Cat# HPA009173; RRID: <a href="#">AB_1079429</a>
anti-GFP (chicken) [1:200]	Aves Labs	Cat# GFP-1020; RRID: <a href="#">AB_10000240</a>
anti-ZO-1 (rat) [1:100]	Millipore	Cat# MABT11; RRID: <a href="#">AB_10616098</a>
anti-ZO-1 (rabbit) [1:50]	ThermoFisher	Cat# 61-7300; RRID: <a href="#">AB_2533938</a>
Goat anti-mouse Alexa Fluor 488 F(ab')2 fragment [1:1000]	ThermoFisher	Cat# A-11017; RRID: <a href="#">AB_2534084</a>
Goat anti-rabbit Alexa Fluor 488 F(ab')2 fragment [1:1000]	ThermoFisher	Cat# A-11070; RRID: <a href="#">AB_2534114</a>
Goat anti-rabbit Alexa Fluor 568 F(ab')2 fragment [1:1000]	ThermoFisher	Cat# A-21069; RRID: <a href="#">AB_253573</a>
Goat anti-chicken Alexa Fluor 488 IgG (H+L) [1:1000]	ThermoFisher	Cat# A-11039; RRID: <a href="#">AB_142924</a>
Goat anti-rat Alexa Fluor 647 IgG (H+L) [1:200]	ThermoFisher	Cat# A-21247; RRID: <a href="#">AB_141778</a>
<b>Bacterial and virus strains</b>		

<i>E. coli</i> DH5-Alpha competent cells	Molecular Biology Resource Core, Vanderbilt Medical Center	Item# DH5 Alpha
<b>Chemicals, peptides, and recombinant proteins</b>		
Alexa Fluor Plus 405 Phalloidin [1:200]	ThermoFisher	Cat# A30104
Alexa Fluor 647 Phalloidin [1:200]	ThermoFisher	Cat# A22287
Janelia Fluor 635 (JF635)	Janelia	N/A
16% Paraformaldehyde	Electron Microscopy Sciences	Cat# 15710
Triton X-100	Sigma	Cat# T8787
ProLong Gold Antifade Reagent	Invitrogen	Cat# P36930
FuGENE 6	Promega	Cat# E2691
Lipofectamine 2000	ThermoFisher	Cat# 11668019
G418 Sulfate	Gold Biotechnology	Cat#G-418-1
Puromycin	Gold Biotechnology	Cat# P-600-100
Antibiotic-antimycotic (anti-anti)	Gibco	Cat# 15240062
Glutaraldehyde 25%	Electron Microscopy Sciences	Cat# 16220
Tannic Acid	Electron Microscopy Sciences	Cat# 21700
Osmium Tetroxide	Electron Microscopy Sciences	Cat# 19112
<b>Experimental models: Cell lines</b>		
LLC-PK1-CL4	Gift from Dr. Carolyn Slayman (Yale University)	N/A
CACO-2 <sub>BBE</sub>	ATCC	Cat# CRL-2102

<b>Experimental models: Organisms/strains</b>			
CDHR2-EGFP mouse	Vanderbilt Genome Editing Resource		N/A
<b>Oligonucleotides</b>			
CDHR2-Fwd: ATGGCCCAGCTATGGCTG	This paper		N/A
CDHR2-Rev: CAGGTCCGTGGTGTCCAGG	This paper		N/A
<b>Recombinant DNA</b>			
pmCherry-Espin (ESPN)	Gift from Dr. James Bartles, NWU		N/A
pLVX-mCherry-Espin (ESPN)	[20]		N/A
pEGFP-N3-CDHR2 (PCDH24-EGFP)	[11]		N/A
pmCherry-N3-CDHR2	Tyska Laboratory		N/A
pEGFP-N3-CDHR5	Tyska Laboratory		N/A
pmCherry-N3-CDHR5	Tyska Laboratory		N/A
pmNEONGreen-β-Actin	Purchased from Allele Biotechnology		Allele ABP-FP- MENEONSA
pHALO-N3-CDHR2	This paper		N/A
<b>Software and algorithms</b>			
FIJI	<a href="https://fiji.sc">https://fiji.sc</a>		N/A
NIS AR Elements Analysis	Nikon ( <a href="https://bit.ly/3fFd8rz">https://bit.ly/3fFd8rz</a> )		N/A
Prism 9	GraphPad ( <a href="https://graphpad.com">https://graphpad.com</a> )		N/A
<b>Other</b>			
MycoAlert PLUS Mycoplasma Detection Kit	Lonza	Cat# LT07-710	
PCR™8/GW/TOPO™ TA Cloning Kit	Invitrogen	Cat# K250020	
Gateway™ Vector Conversion System	Invitrogen	Cat# 11828029	

35 mm #1.5 glass bottom dishes	CellVis	Cat# D35-20-1.5-N
--------------------------------	---------	-------------------

608

609 **Animal studies**

610 Animal experiments were carried out in accordance with Vanderbilt University Medical  
 611 Center Institutional Animal Care and Use Committee guidelines under IACUC Protocol  
 612 ID#: M1600206-02.

613

614 **CDHR2-EGFP mouse**

615 Created in collaboration with the Vanderbilt Genome Editing Resource. A C57Bl/6N strain  
 616 containing a *CDHR2* C-terminal EGFP sequence insertion. [crRNA sequence:  
 617 TGGACACCACAGATCTGTGA] Ribonucleoprotein complexes containing crRNA and WT  
 618 SpCas9 protein were targeted to the C-terminus of *CDHR2* were assembled and injected  
 619 with a single stranded 944 nt DNA donor into 1-cell C57Bl/6N embryos. crRNA, tracrRNA,  
 620 and WT SpCas9 protein was sourced from MilliporeSigma. The single stranded DNA was  
 621 produced by Genewiz. Pups were screened for CDHR2-EGFP sequence insertions by  
 622 PCR and validated by Sanger sequencing.

623

624 **Frozen Section Tissue Preparation**

625 The proximal segment (duodenum to jejunum) of the mouse intestinal tube was excised  
 626 and flushed with cold 1X phosphate-buffered saline (PBS). One end of the tube was  
 627 clamped with a hemostat and the tube was filled with room temperature 2%  
 628 paraformaldehyde (PFA) (Electron Microscopy Sciences) with a syringe and metal  
 629 cannula. The other end of the tube was clamped with a hemostat and the tissue was laid  
 630 in a petri dish containing excess 2% PFA and incubated for 15 minutes at room  
 631 temperature. Hemostats were removed and the tissue was cut lengthwise into one flat  
 632 piece. Tissue was then sub dissected into ~2mm<sup>2</sup> pieces and fixed for an additional 30  
 633 minutes in a vial of 2% PFA at room temperature. After fixation, the tissue was washed 3  
 634 times with PBS and then placed, villi-side down, into a vial of cold 30% sucrose/1%  
 635 sodium azide. The tissue was placed at 4°C, overnight until sections sank to the bottom  
 636 of the tube. The next day, sections were passed through 3 separate blocks of optimal

637 cutting temperature (OCT) compound (Electron Microscopy Sciences) to wash off the  
638 sucrose solution, oriented with villi parallel to the lab bench in a fresh block of OCT, and  
639 snap frozen in dry ice-cooled acetone. Samples were cut into 10 µm thin sections using  
640 a Leica CM1950 cryostat and mounted on plasma-cleaned #1.5H precision coverslips  
641 (Thorlabs). Coverslips were stored at -20°C until staining.

642

#### 643 **Frozen Section Immunofluorescence**

644 Coverslips were thawed to room temperature and rinsed twice with 1X PBS to remove  
645 OCT. Sections were permeabilized with 0.2% Triton X-100 (diluted in PBS) for 10 minutes  
646 at room temperature. Sections were then rinsed once with PBS at room temperature and  
647 blocked in 10% bovine serum albumin (BSA) for 2 hours at 37°C in a humidified chamber.  
648 After rinsing with PBS, primary antibody (diluted in 1% BSA) was applied overnight at 4°C  
649 in a humidified chamber. The next day, sections were rinsed with 1X PBS 4 times and  
650 secondary antibody (diluted in 1% BSA) was applied for 2 hours at room temperature in  
651 a dark, humidified chamber. Sections were rinsed 4 times with 1X PBS and coverslips  
652 were mounted onto glass slides with ProLong Gold. The following antibodies and dilutions  
653 were used for EGFP-CDHR2 mouse frozen section staining: anti-GFP (chicken Aves  
654 #GFP-1020), 1:200; anti-CDHR5 (rabbit, Sigma #HPA009173), 1:250; anti-ZO-1 clone  
655 R40.76 (rat, EMD Millipore Sigma #MABT11), 1:100; Alexa Fluor goat anti-chicken 488  
656 (Invitrogen #A-11039), 1:1000; Alexa Fluor F(ab')2 fragment goat anti-rabbit 568  
657 (Invitrogen #A21069), 1:1000; Alexa Fluor goat anti-rat 647 (Invitrogen #A21247), 1:200;  
658 and Alexa Fluor Plus 405 Phalloidin (Invitrogen #A30104), 1:200 for actin staining. The  
659 secondary antibodies, not including phalloidin, were spun down for 10 minutes at 4°C and  
660 21 x g prior to using.

661

#### 662 **Cell Culture**

663 LLC-PK1-CL4 (porcine kidney proximal tubule) cells were grown in 1X high glucose  
664 DMEM containing 2mM L-glutamine (Corning #10-013-CV) supplemented with 1% L-  
665 glutamine (Corning # 25-005-CI) and 10% fetal bovine serum (FBS) (R&D Systems) while  
666 CACO-2<sub>BBE</sub> (human colonic adenocarcinoma) cells were grown in the same medium but  
667 supplemented with 20% FBS. Cells were maintained in culture incubated at 37°C and 5%

668 CO<sub>2</sub>. Cells were tested for mycoplasma using the MycoAlert PLUS Mycoplasma  
669 Detection Kit (Lonza #LT07-710).

670

## 671 **Cloning and Constructs**

672 A C terminally tagged pHALO-N3-CDHR2 (CDHR2-HALO) construct was generated by  
673 taking full length CDHR2 via PCR from pEGFP-N3-PCDH24 (CDHR2-EGFP) with the  
674 primers CDHR2-Fwd: ATGGCCCAGCTATGGCTG and CDHR2-Rev:  
675 CAGGTCCGTGGTGTCCAGG. The product was then TOPO cloned into the  
676 pCR8/GW/TOPO vector (Invitrogen #K250020) and then placed into the pHALO-N3  
677 backbone, adapted for Gateway cloning using the Gateway conversion kit (Invitrogen  
678 #11828029). All other overexpression constructs listed in this paper were previously  
679 created and/or reported as noted in the key resources table.

680

## 681 **Cell Line Generation**

682 Cells expressing one plasmid were transfected with FuGENE 6 (Promega #E2691) at a  
683 FuGENE:DNA ( $\mu$ L: $\mu$ g) ratio of 3:1 following the reagent protocol in a T25 cell culture flask.  
684 The next day, all cells were split up to a T75 flask with the addition of 1mg/mL G418  
685 sulfate for antibiotic selection. Cells were maintained in culture under constant G418  
686 selection to create a stably expressing cell line. Cells co-expressing two plasmids were  
687 transiently transfected with Lipofectamine 2000 (Invitrogen #11668019) according to the  
688 manufacturer's protocol. The next day, cells were split to plasma-cleaned 35mm glass  
689 bottom dishes (CellVis #D35-20-1.5-N) for subsequent imaging. The EGFP-  
690 EPS8/mCherry-ESPN CL4 stable cell line was previously created [20] by transducing a  
691 G418-selected EGFP-EPS8 stable cell line with lentiviral mCherry-ESPN followed by 10  
692  $\mu$ g/mL puromycin selection. See citation for detailed protocol. The Halo-CDHR2/EGFP-  
693 CDHR5 co-expressing CL4 cells were a transient transfection, and not stably selected.

694

## 695 **Cell Immunofluorescence**

696 Prior to fixation and staining, CL4 and CACO-2<sub>BBE</sub> cells were grown to  $n$  days post-  
697 confluent (DPC) on acid-washed 22x22 mm #1.5H coverslips (Globe Scientific) in a 6-  
698 well plate to a time point with apical polarity representative of their native tissue, 3 DPC

699 and 12 DPC, respectively. First, cells were rinsed in warm 1X PBS and fixed in 4% PFA  
700 for 15 minutes at 37°C. Cells were then washed three times, 5 minutes each, with 1X  
701 PBS and permeabilized with 0.1% Triton X-100 for 10 minutes at room temperature. 5%  
702 BSA was added for 1 hour at 37°C as blocking solution. After rinsing with 1X PBS, primary  
703 antibody (diluted in 1% BSA) was added for 1 hour at 37°C. Labeling with primary  
704 antibody was followed by washing 4 times, 5 minutes each, with 1X PBS. Secondary  
705 antibody (diluted in 1% BSA) was then applied for 1 hour at room temperature in the dark.  
706 After incubation in secondary antibody, cells were washed 4 times, 5 minutes each with  
707 1X PBS and coverslips were mounted on glass slides with ProLong Gold. The following  
708 antibodies and dilutions were used for cell staining: anti-PCLKC (CDHR2) (mouse,  
709 Abnova #H00054825-M01), 1:25; anti-CDHR5 (Rabbit, Sigma #HPA009173), 1:250; anti-  
710 ZO-1 clone R40.76 in CL4 (rat, EMD Millipore Sigma #MABT11), 1:100; anti-ZO-1 in  
711 CACO-2<sub>BBE</sub> (rabbit, Invitrogen #61-7300), 1:50; Alexa Fluor F(ab')2 fragment goat anti-  
712 mouse 488 (Invitrogen #A11017) and goat anti-rabbit 568 (Invitrogen #A21069), 1:1000;  
713 Alexa Fluor goat anti-rat 647 (Invitrogen #A21247), 1:200; and Alexa Fluor Plus 405  
714 Phalloidin (Invitrogen # A30104) or Alexa Fluor 647 Phalloidin (Invitrogen # A22287),  
715 1:200 for actin staining. The secondary antibodies, not including phalloidin, were spun  
716 down for 10 minutes at 4°C and 21 x g prior to using.

717

### 718 **Fluorescence-activated Cell Sorting (FACS)**

719 Cells were spun down into a pellet and resuspended in “pre-sort medium” containing  
720 Phenol free 1X DMEM (Gibco #21063-029) plus 5% FBS, and 1% L-glutamine. Cells were  
721 sorted by Vanderbilt University Medical Center’s Flow Cytometry Shared Resource on a  
722 5-Laser FACS Aria III system with a 100 µm sized nozzle. All fluorescent positive cells  
723 (Fig. S3) were deposited into a single well of a 6-well plate containing “post-sort medium”  
724 of 1X DMEM (Corning #10-013-CV) with Phenol red, 10% FBS, 1% L-glutamine, and  
725 10µL/mL anti-anti (Gibco #15240062). 24 hours post-sort, the media was changed to CL4  
726 culture media (as detailed in cell culture methods) and 1 mg/mL G418 was added for  
727 maintaining stable plasmid overexpression. Sorted cell lines were maintained in this  
728 media and under antibiotic selection.

729

730 **Cell Mixing Experiments**

731 Fluorescently sorted CL4 cell populations were grown independently and under G418  
732 antibiotic selective pressure to ~80% confluence, trypsinized, and resuspended in CL4  
733 media to a density of ~850,000 cells/mL. 250 µL of each cell population were seeded in  
734 plasma-cleaned glass-bottom dishes or onto acid washed coverslips at a density of  
735 ~400,000 total cells at a mixing ratio of 1:1 (e.g. CDHR2-EGFP cells were mixed with  
736 CDHR5-mCherry cells). Immediately after seeding, cell populations were thoroughly  
737 mixed by pipette. Cells were grown to 3DPC for fixed cell staining or for 1 day for live cell  
738 imaging (FRAP).

739

740 **Fixed Sample Microscopy**

741 Laser scanning confocal microscopy was performed on a Nikon A1 microscope equipped  
742 with 488 nm, 568 nm, and 647 nm LASERs. Mixed CL4 cell populations for linescan  
743 analysis were imaged using a Plan Apo 40x/1.3 NA oil immersion objective. CACO-2<sub>BBE</sub>  
744 cells were imaged using an Apo TIRF 100x/1.49 NA TIRF oil immersion objective.  
745 Structured illumination microscopy (SIM) was used for imaging frozen tissue sections and  
746 fixed cells with a Nikon N-SIM equipped with 405, 488, 468, and 647 nm LASERs, an  
747 Andor DU-897 EMCCD camera, and a TIRF 100X/1.49 NA TIRF oil immersion objective.  
748 All SIM images were reconstructed using Nikon Elements software.

749

750 **Live Imaging Microscopy**

751 Prior to live cell imaging, cells growing in 35mm glass bottom dishes were rinsed once  
752 with 1X DPBS (Corning #21-031-CV). FluoroBrite imaging media (Gibco #A18967-01)  
753 supplemented with 10% FBS and 1% L-glutamine was added to the dish. For CL4 cells  
754 expressing Halo-CDHR2, Janelia Fluor 635 dye (Janelia) was added to the FluoroBrite  
755 media at a concentration of 50 nM for 1 hour at 37°C immediately prior to imaging.  
756 Spinning disk confocal microscopy was performed using a Nikon Ti2 inverted light  
757 microscope with a Yokogawa CSU-X1 spinning disk head, a Photometrics Prime 95B or  
758 Hamamatsu Fusion BT sCMOS camera, and three excitation LASERs (488, 568 and 647  
759 nm). A 100X/1.49 NA TIRF oil immersion objective was used for all acquisitions. A stage  
760 incubator (Tokai Hit) maintained cells in a humidified environment at 37°C with 5% CO<sub>2</sub>.

761

762 **Fluorescence Recovery after Photobleaching (FRAP)**

763 A square ROI was drawn in Nikon Elements at marginal and/or medial microvilli regions.  
764 A stimulating 405 nm LASER controlled by a Bruker mini-scanner set at 70% power and  
765 a dwell time of 40 us was targeted to each ROI after the first 3 frames of the movie  
766 acquisition. Two ND time acquisitions were used for imaging fluorescence recovery at  
767 intervals of 15 s for 3 minutes, followed by intervals of 30 s for 10 minutes.

768

769 **Electron Microscopy – CACO-2<sub>BBE</sub> and LLC-PK1-CL4 cells and tissue**

770 To prepare samples, cells were plated on glass coverslips washed once with warm SEM  
771 buffer (0.1M HEPES, pH 7.3) supplemented with 2 mM CaCl<sub>2</sub>, then fixed with 2.5%  
772 glutaraldehyde and then 4% paraformaldehyde in SEM buffer supplemented with 2mM  
773 CaCl<sub>2</sub>. Samples were washed in SEM buffer, then incubated in 1% tannic acid, washed  
774 with ddH<sub>2</sub>O, incubated with 1% OsO<sub>4</sub>, washed with ddH<sub>2</sub>O, incubated with 1% uranyl  
775 acetate, then washed with ddH<sub>2</sub>O. Samples were dehydrated in a graded ethanol series.  
776 Sampels were then dried using critical point drying and mounted on aluminum stubs and  
777 coated with gold/palladium using a sputter coater. SEM imaging was performed using  
778 Quanta 250 Environmental-SEM operated in high vacuum mode with an accelerating  
779 voltage of 5–10 kV, or imaged on a Zeiss Crossbeam 550 at 2keV. All reagents were  
780 purchased from Electron Microscopy Sciences. For more detailed methods, see [28].  
781 TEM of mouse intestine (Fig. S1B) was performed as previously described [14]

782

783 **Electron Microscopy – Crypt-villus axis**

784 For SEM imaging of intestinal sections, immediately after euthanasia, ~5 mm murine  
785 duodenal sections were quickly fixed in a large volume (10mL) of 2.5% glutaraldehyde  
786 and 4% paraformaldehyde in SEM buffer (described above). Sections were then washed  
787 in SEM buffer prior to embedding in Tissue-Tek OCT compound (Sakura Finetek #4583).  
788 To ensure stable support of the complex architecture within the explant lumens, samples  
789 were gently moved through 3 rounds of fresh OCT compound with gentle manipulation to  
790 ensure penetration of the OCT. Samples were then placed in cryomolds (with OCT) and  
791 frozen over a dry ice/ethanol slurry. Molds were stored at -80C once fully frozen. Frozen

792 explants were subsequently sectioned on a Leica CM1950 cryostat at 50 $\mu$ m/section and  
793 melted onto stainless steel AFM specimen discs (Electron Microscopy Sciences). Next,  
794 explant sections and disks were immersed in 1% OsO<sub>4</sub>, washed in ddH<sub>2</sub>O, then  
795 dehydrated through graded ethanol series. Of note, it was most common to experience  
796 detachment of the section from the AFM disk during the OsO<sub>4</sub> and dehydration steps.  
797 Detached sections were recovered and gently adhered to an aluminum SEM specimen  
798 stub via conductive adhesive tab. SEM imaging was performed on a Quanta 250  
799 environmental SEM, as described above.

800

### 801 **Quantification and Statistical Analysis**

802 *Microvilli Orientation Measurements.* In Fiji, the first frames of three independent  
803 mCherry-ESPN CL4 cell movies were used for orientation measurements shown in Fig.  
804 2B. A thin, rectangular ROI (height 12 pixels) was drawn across 2+ cells to encompass  
805 both marginal and medial areas (sample ROI Fig 2A, dotted box). The ROI hyperstack  
806 was duplicated and 3D projected with rotation around the X axis. Using the Angle tool, a  
807 line was drawn down the length of each microvillus (dotted lines, Fig. 2B) with the angle  
808 base parallel to the cell surface (solid lines Fig. 2B). Angle measurements were plotted in  
809 Prism in a column chart and mean marginal and medial angles were compared using a  
810 Welch's unpaired t-test.

811

812 *Temporal Color Coding.* Time frames for every 3 minutes were selected (18 total frames).  
813 Using the Temporal-Color Code function in Fiji, the ESPN channel was coded (start frame  
814 1, end frame 18) using the Spectrum LUT (Fig. 3B).

815

816 *Microvilli tracking using EGFP-EPS8 puncta.* Denoised and deconvolved 3D movies were  
817 converted into max intensity projections in the Z plane. Next, a binary via the spot  
818 detection tool was applied to the FITC channel (EPS8 signal) with a diameter of 260 nm  
819 and a contrast value of 25 to threshold EPS8 puncta representing individual microvilli in  
820 the ROI (medial or marginal). Tracking parameters did not allow for the detection of new  
821 tracks after the first frame, allowed for a maximum of 3 gaps in a given track, and a  
822 standard deviation multiplier of 2. Using the tracking tool, binaries, representing EPS8

823 puncta, were tracked and any points lying outside of the ROI were deselected. Track data,  
824 time and X Y positions, were then exported to Excel and analyzed and plotted in Prism  
825 as radial X Y positions over time by subtracting each position in X or Y from the respective  
826 point position at time 0, making the first position (0,0) (Fig 3C and 3F). Three independent  
827 live cell imaging experiments were used for the analysis.

828

829 *Mean Square Displacement.* With the same X,Y EPS8 puncta trajectories described  
830 above, an Excel spreadsheet was used to calculate the mean square displacement of  
831 each tracked microvillus over 15 s intervals across 5 minutes as us and others have done  
832 previously [28, 49-51]. A line was fitted to each MSD curve using the simple linear  
833 regression model in Prism which provided the slopes presented on the plots in Fig. 3E  
834 and H.

835

836 *Cell Mixing Linescans.* Using Fiji, a segmented line with a width of 6 was drawn across  
837 mixed cell interfaces to encapsulate signal at the mixed cell (marginal) interfaces. Lines  
838 with a minimum length of 20  $\mu\text{m}$  and maximum length of 75  $\mu\text{m}$  were used in analysis.  
839 Fig. 5 shows one representative linescan from the large dataset for each cell mixing  
840 scenario, with line length ( $\mu\text{m}$ ) shown on the X axis and mCherry and EGFP construct  
841 intensities on the Y axis. Intensities were normalized from 0 to 1 in Prism with 0 being the  
842 lowest gray value in the linescan and 1 being the highest. The residual plots shown were  
843 calculated from the respective representative linescan by subtracting mCherry intensity  
844 from EGFP intensity at each length in X. 30 individual linescans from each cell mixing  
845 scenario were plotted on their own XY correlation plot in Prism. Combined Pearson's r  
846 values from the 30 individual correlations were plotted in Fig 5K, and mean r values were  
847 compared in Prism using an Ordinary one-way ANOVA with multiple comparisons.

848

849 *FRAP Fraction Recovery Analysis.* A background ROI and reference ROI were used to  
850 account for photobleaching and background fluorescence in both channels. Fraction  
851 recovery over time was calculated from  $\frac{\text{(Bleached ROI}-\text{Background)}}{\text{(Reference ROI}-\text{Background})}}$ . Recovery curves were  
852 fitted with a two-phase association equation in Prism and the immobile fraction was  
853 calculated from 1 minus the plateau. Images shown in Fig. 6 were denoised and

854 deconvolved in Nikon Elements for presentation clarity, however all analyzed  
855 measurements presented in the FRAP plots were taken from raw, unprocessed movies.

856

857 *Mean ESPN Intensity Measurements.* In Nikon Elements, the movie was projected in Z  
858 to create a maximum intensity projection. For Fig. 7D, at 0 hr and 24 hr a ring ROI was  
859 drawn encompassing each marginal zone and separate circular ROI was drawn to  
860 encompass the medial zone of 10 cells. Mean mCherry-ESPN intensity was measured  
861 for each cell at the marginal and medial zones. Delta represents the change in mCherry-  
862 ESPN mean intensity from the 0 hr time point to the 24 hr time point.

863

864 **REFERENCES**

- 865 1. Coudrier, E., D. Kerjaschki, and D. Louvard, *Cytoskeleton organization and*  
866 *submembranous interactions in intestinal and renal brush borders.* Kidney Int,  
867 1988. **34**(3): p. 309-20.
- 868 2. Sauvanet, C., et al., *Structure, regulation, and functional diversity of microvilli on*  
869 *the apical domain of epithelial cells.* Annu Rev Cell Dev Biol, 2015. **31**: p. 593-621.
- 870 3. Mooseker, M.S. and L.G. Tilney, *Organization of an actin filament-membrane*  
871 *complex. Filament polarity and membrane attachment in the microvilli of intestinal*  
872 *epithelial cells.* J Cell Biol, 1975. **67**(3): p. 725-43.
- 873 4. Ohta, K., et al., *Helical arrangement of filaments in microvillar actin bundles.* J  
874 Struct Biol, 2012. **177**(2): p. 513-9.
- 875 5. Helander, H.F. and L. Fandriks, *Surface area of the digestive tract - revisited.*  
876 Scand J Gastroenterol, 2014. **49**(6): p. 681-9.
- 877 6. Wessely, O., et al., *The bigger the better: determining nephron size in kidney.*  
878 Pediatr Nephrol, 2014. **29**(4): p. 525-30.
- 879 7. Delacour, D., et al., *Plasticity of the brush border - the yin and yang of intestinal*  
880 *homeostasis.* Nat Rev Gastroenterol Hepatol, 2016. **13**(3): p. 161-74.
- 881 8. Fath, K.R., S.D. Obenauf, and D.R. Burgess, *Cytoskeletal protein and mRNA*  
882 *accumulation during brush border formation in adult chicken enterocytes.*  
883 Development, 1990. **109**(2): p. 449-59.
- 884 9. Specian, R.D. and M.R. Neutra, *The surface topography of the colonic crypt in*  
885 *rabbit and monkey.* Am J Anat, 1981. **160**(4): p. 461-72.
- 886 10. Rice, W.L., et al., *High resolution helium ion scanning microscopy of the rat kidney.*  
887 PLoS One, 2013. **8**(3): p. e57051.
- 888 11. Crawley, S.W., et al., *Intestinal brush border assembly driven by protocadherin-*  
889 *based intermicrovillar adhesion.* Cell, 2014. **157**(2): p. 433-446.
- 890 12. Weck, M.L., et al., *Myosin-7b Promotes Distal Tip Localization of the*  
891 *Intermicrovillar Adhesion Complex.* Curr Biol, 2016. **26**(20): p. 2717-2728.
- 892 13. Crawley, S.W., et al., *ANKS4B Is Essential for Intermicrovillar Adhesion Complex*  
893 *Formation.* Dev Cell, 2016. **36**(2): p. 190-200.
- 894 14. Pinette, J.A., et al., *Brush border protocadherin CDHR2 promotes the elongation*  
895 *and maximized packing of microvilli in vivo.* Mol Biol Cell, 2019. **30**(1): p. 108-118.
- 896 15. McConnell, R.E., et al., *Proteomic analysis of the enterocyte brush border.* Am J  
897 Physiol Gastrointest Liver Physiol, 2011. **300**(5): p. G914-26.

- 898 16. Gray, M.E., et al., *Heterophilic and homophilic cadherin interactions in intestinal*  
899 *intermicrovillar links are species dependent.* PLoS Biol, 2021. **19**(12): p. e3001463.
- 900 17. Li, J., et al., *Mechanistic Basis of Organization of the Harmonin/USH1C-Mediated*  
901 *Brush Border Microvilli Tip-Link Complex.* Dev Cell, 2016. **36**(2): p. 179-89.
- 902 18. Li, J., et al., *Structure of Myo7b/USH1C complex suggests a general PDZ domain*  
903 *binding mode by MyTH4-FERM myosins.* Proc Natl Acad Sci U S A, 2017. **114**(19):  
904 p. E3776-E3785.
- 905 19. Choi, M.S., et al., *The small EF-hand protein CALML4 functions as a critical*  
906 *myosin light chain within the intermicrovillar adhesion complex.* J Biol Chem, 2020.  
907 **295**(28): p. 9281-9296.
- 908 20. Gaeta, I.M., et al., *Direct visualization of epithelial microvilli biogenesis.* Curr Biol,  
909 2021. **31**(12): p. 2561-2575 e6.
- 910 21. Higgs, H.N., *There goes the neighbourhood: Eps8 joins the barbed-end crowd.* Nat  
911 Cell Biol, 2004. **6**(12): p. 1147-9.
- 912 22. Manor, U., et al., *Regulation of stereocilia length by myosin XVa and whirlin*  
913 *depends on the actin-regulatory protein Eps8.* Curr Biol, 2011. **21**(2): p. 167-72.
- 914 23. Disanza, A., et al., *Regulation of cell shape by Cdc42 is mediated by the synergic*  
915 *actin-bundling activity of the Eps8-IRSp53 complex.* Nat Cell Biol, 2006. **8**(12): p.  
916 1337-47.
- 917 24. Croce, A., et al., *A novel actin barbed-end-capping activity in EPS-8 regulates*  
918 *apical morphogenesis in intestinal cells of Caenorhabditis elegans.* Nat Cell Biol,  
919 2004. **6**(12): p. 1173-9.
- 920 25. Postema, M.M., et al., *IRTKS (BAIAP2L1) Elongates Epithelial Microvilli Using*  
921 *EPS8-Dependent and Independent Mechanisms.* Curr Biol, 2018. **28**(18): p. 2876-  
922 2888 e4.
- 923 26. Tocchetti, A., et al., *Loss of the actin remodeler Eps8 causes intestinal defects and*  
924 *improved metabolic status in mice.* PLoS One, 2010. **5**(3): p. e9468.
- 925 27. Zampini, V., et al., *Eps8 regulates hair bundle length and functional maturation of*  
926 *mammalian auditory hair cells.* PLoS Biol, 2011. **9**(4): p. e1001048.
- 927 28. Meenderink, L.M., et al., *Actin Dynamics Drive Microvillar Motility and Clustering*  
928 *during Brush Border Assembly.* Dev Cell, 2019. **50**(5): p. 545-556 e4.
- 929 29. Peterson, M.D. and M.S. Mooseker, *Characterization of the enterocyte-like brush*  
930 *border cytoskeleton of the C2BBe clones of the human intestinal cell line, Caco-2.*  
931 *J Cell Sci, 1992. **102** ( Pt 3): p. 581-600.*

- 932 30. Nielsen, R., et al., *Characterization of a kidney proximal tubule cell line, LLC-PK1,*  
933 *expressing endocytotic active megalin.* J Am Soc Nephrol, 1998. **9**(10): p. 1767-  
934 76.
- 935 31. Bartles, J.R., et al., *Small espin: a third actin-bundling protein and potential forked*  
936 *protein ortholog in brush border microvilli.* J Cell Biol, 1998. **143**(1): p. 107-19.
- 937 32. Loomis, P.A., et al., *Espin cross-links cause the elongation of microvillus-type*  
938 *parallel actin bundles in vivo.* J Cell Biol, 2003. **163**(5): p. 1045-55.
- 939 33. Stevenson, B.R., et al., *Identification of ZO-1: a high molecular weight polypeptide*  
940 *associated with the tight junction (zonula occludens) in a variety of epithelia.* J Cell  
941 Biol, 1986. **103**(3): p. 755-66.
- 942 34. Trier, J.S., *Studies on Small Intestinal Crypt Epithelium. I. The Fine Structure of*  
943 *the Crypt Epithelium of the Proximal Small Intestine of Fasting Humans.* J Cell Biol,  
944 1963. **18**(3): p. 599-620.
- 945 35. Li, J., et al., *Culture and characterization of chicken small intestinal crypts.* Poult  
946 Sci, 2018. **97**(5): p. 1536-1543.
- 947 36. Wu, S.K., et al., *Cortical F-actin stabilization generates apical-lateral patterns of*  
948 *junctional contractility that integrate cells into epithelia.* Nat Cell Biol, 2014. **16**(2):  
949 p. 167-78.
- 950 37. Vanslembrouck, B., et al., *Microscopic Visualization of Cell-Cell Adhesion*  
951 *Complexes at Micro and Nanoscale.* Front Cell Dev Biol, 2022. **10**: p. 819534.
- 952 38. Sokurenko, E.V., V. Vogel, and W.E. Thomas, *Catch-bond mechanism of force-*  
953 *enhanced adhesion: counterintuitive, elusive, but ... widespread?* Cell Host  
954 Microbe, 2008. **4**(4): p. 314-23.
- 955 39. Thomas, W., *For catch bonds, it all hinges on the interdomain region.* J Cell Biol,  
956 2006. **174**(7): p. 911-3.
- 957 40. Rakshit, S., et al., *Ideal, catch, and slip bonds in cadherin adhesion.* Proc Natl  
958 Acad Sci U S A, 2012. **109**(46): p. 18815-20.
- 959 41. Thomas, W., *Catch bonds in adhesion.* Annu Rev Biomed Eng, 2008. **10**: p. 39-  
960 57.
- 961 42. Guo, B. and W.H. Guilford, *Mechanics of actomyosin bonds in different nucleotide*  
962 *states are tuned to muscle contraction.* Proc Natl Acad Sci U S A, 2006. **103**(26):  
963 p. 9844-9.
- 964 43. Kong, F., et al., *Demonstration of catch bonds between an integrin and its ligand.*  
965 J Cell Biol, 2009. **185**(7): p. 1275-84.

- 966 44. VanDussen, K.L., et al., *Abnormal Small Intestinal Epithelial Microvilli in Patients*  
967 *With Crohn's Disease*. *Gastroenterology*, 2018. **155**(3): p. 815-828.
- 968 45. McGuckin, M.A., et al., *Intestinal barrier dysfunction in inflammatory bowel*  
969 *diseases*. *Inflamm Bowel Dis*, 2009. **15**(1): p. 100-13.
- 970 46. Velle, K.B. and K.G. Campellone, *Extracellular motility and cell-to-cell transmission*  
971 *of enterohemorrhagic E. coli is driven by EspFU-mediated actin assembly*. *PLoS*  
972 *Pathog*, 2017. **13**(8): p. e1006501.
- 973 47. In, J., et al., *Enterohemorrhagic Escherichia coli reduce mucus and intermicrovillar*  
974 *bridges in human stem cell-derived colonoids*. *Cell Mol Gastroenterol Hepatol*,  
975 2016. **2**(1): p. 48-62 e3.
- 976 48. Pedersen, G.A., et al., *The basolateral vesicle sorting machinery and basolateral*  
977 *proteins are recruited to the site of enteropathogenic E. coli microcolony growth at*  
978 *the apical membrane*. *PLoS One*, 2017. **12**(6): p. e0179122.
- 979 49. Qian, H., M.P. Sheetz, and E.L. Elson, *Single particle tracking. Analysis of diffusion*  
980 *and flow in two-dimensional systems*. *Biophys J*, 1991. **60**(4): p. 910-21.
- 981 50. Berg, H.C., *Random walks in biology*. 1993, Princeton: Princeton University Press.
- 982 51. Sheetz, M.P., et al., *Nanometre-level analysis demonstrates that lipid flow does*  
983 *not drive membrane glycoprotein movements*. *Nature*, 1989. **340**(6231): p. 284-8.
- 984
- 985

986 **SUPPLEMENTAL FIGURE LEGENDS**

987 **Figure S1: Microvilli of mature epithelial cells are continuous across the monolayer**  
988 **surface.** **(A)** SEM of mouse small intestine showing an *en face* view of microvilli on  
989 neighboring enterocytes. The dashed box represents a zoom of a single enterocyte cell  
990 and its neighbors. **(B)** Transmission electron micrograph (TEM) of mouse small intestine  
991 showing a lateral view of microvilli. Dashed box represents the zoom of a cell-cell junction  
992 (white arrow) with neighboring cell microvilli appearing continuous across the interface  
993 (black arrow). Scale bars: 4  $\mu\text{m}$  (A), 1  $\mu\text{m}$  (A, zoom), 5  $\mu\text{m}$  (B), 500 nm (B, zoom).

994

995 **Figure S2: High-resolution imaging of adhesion complex interfaces in mixed CL4**  
996 **cell populations.** **(A)** FACS profiles of the four stable CL4 cell lines expressing C-  
997 terminal mCherry or EGFP tagged CDHR2 or CDHR5 as marked on the top axis of the  
998 graph. 3D Volume SIM images of mixed **(B)** heterophilic; CDHR5-mCherry and CDHR2-  
999 EGFP, **(C)** homophilic; CDHR2-EGFP and mCherry-CDHR5, and **(D)** homophilic;  
1000 CDHR5-mCherry and CDHR5-EGFP CL4 cells. Dashed boxes outlined in B-D represent  
1001 zooms shown in bottom panel, respectfully. White arrows in zoom under (B) point to  
1002 instances of robust microvilli alignment at cell margins, which are absent in the homophilic  
1003 mixing scenarios. Scales as marked.

1004

**Fig. S1**

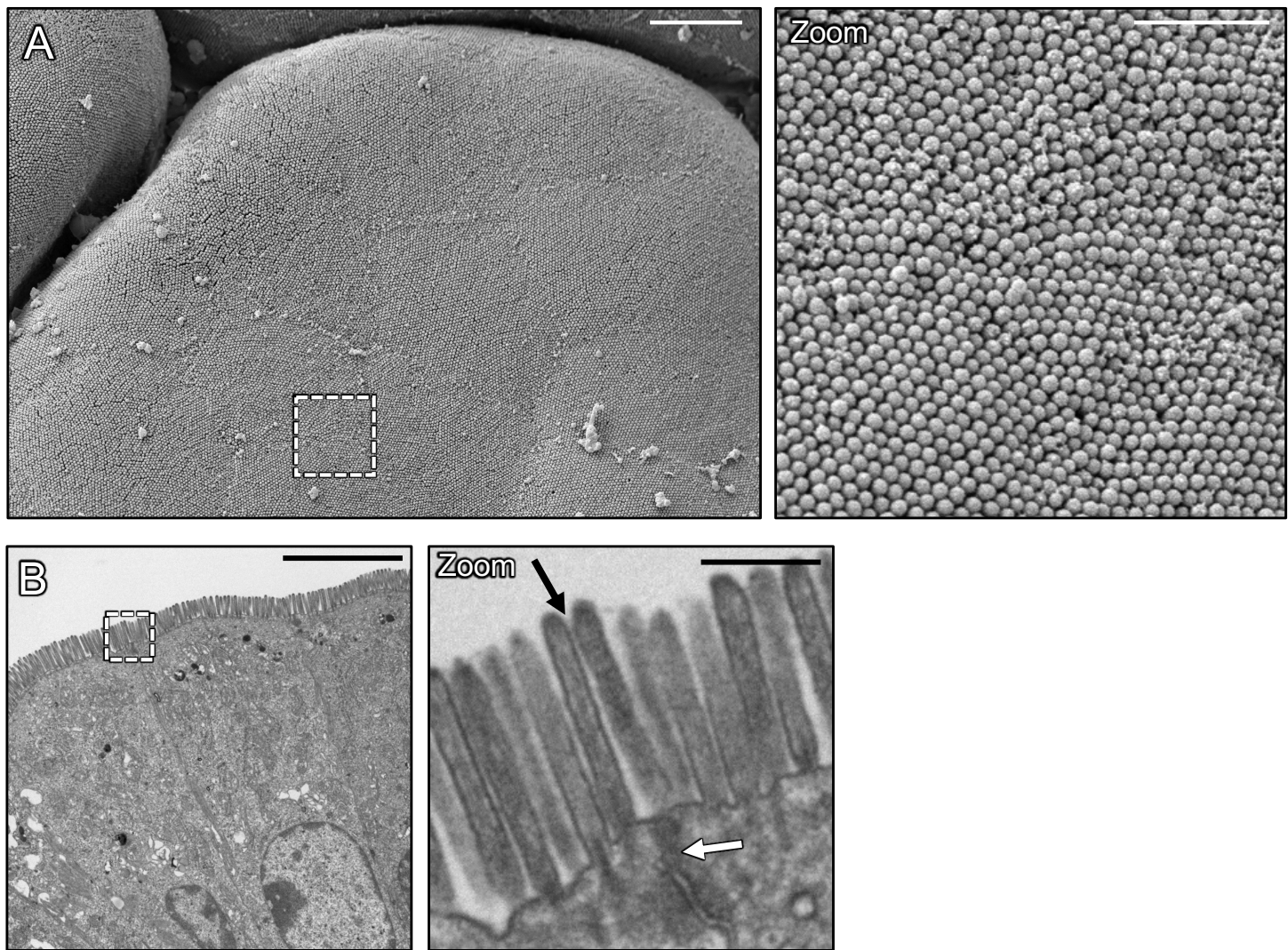
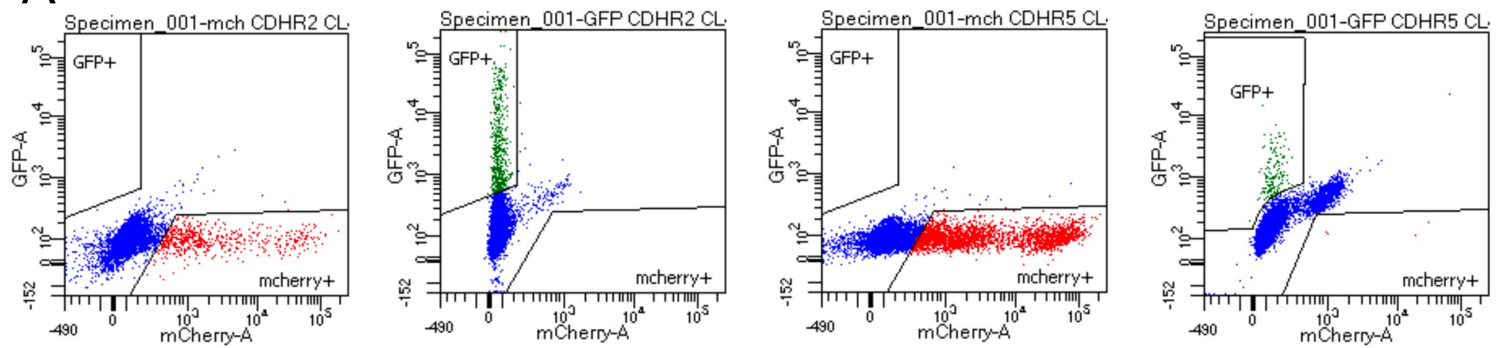
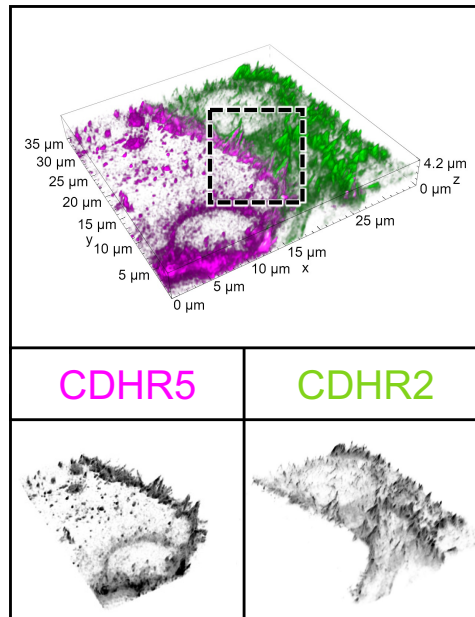


# Fig. S2

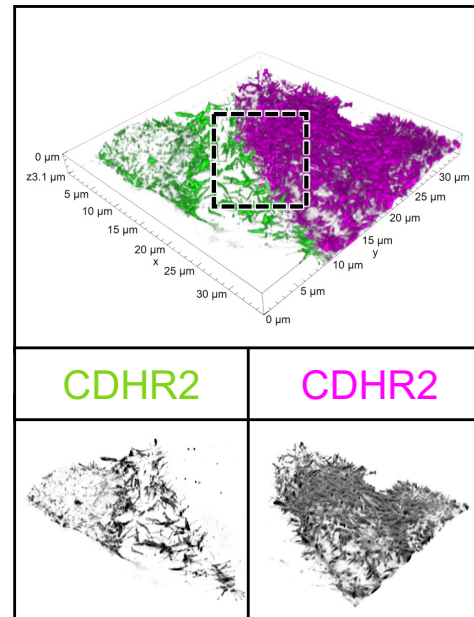
A



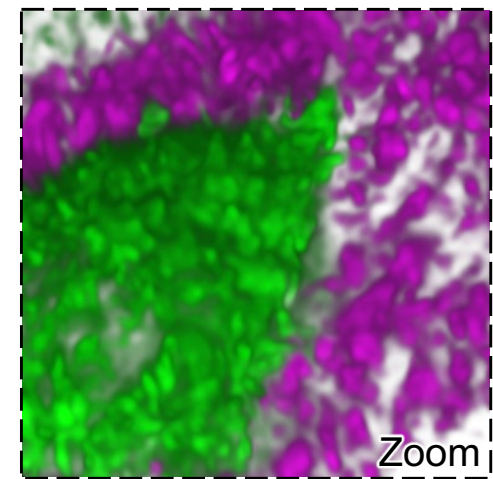
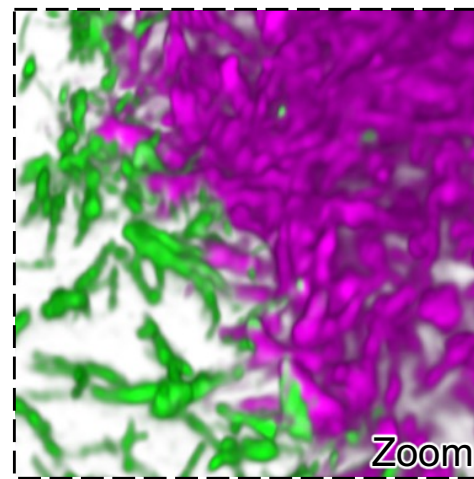
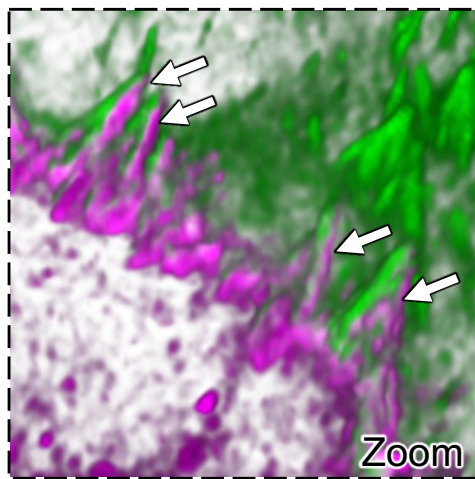
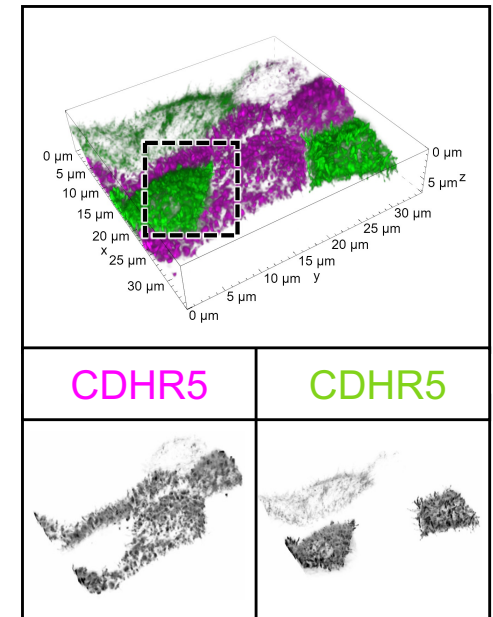
B Heterophilic



C Homophilic – CDHR2



D Homophilic – CDHR5



1005 **SUPPLEMENTAL VIDEO LEGENDS**

1006 **Video S1: Microvilli adopt an orientation perpendicular to the cell surface upon**  
1007 **reaching the cell margins.** 3D volume projection depth coded in Z of live mCherry-ESPN  
1008 expressing CL4 cells. Spinning disk confocal movie taken over 2 hours with 2-minute  
1009 intervals of the microvilli cluster marked in Fig 2C, and D. Arrow follows a cluster of medial  
1010 microvilli that transition to a vertical orientation upon reaching the marginal cell area (as  
1011 marked by Z-depth color profile). Scale bar: 3  $\mu$ m.

1012

1013 **Video S2: Marginal heterophilic adhesion complexes have low signal recovery,**  
1014 **suggesting high complex stability.** Mixed CL4 cells expressing CDHR2-EGFP (green)  
1015 and CDHR5-mCherry (magenta) photobleached at two marginal ROIs; 30s intervals  
1016 shown. Scale bar: 5  $\mu$ m.

1017

1018 **Video S3: Medial heterophilic adhesion complexes have higher signal recovery,**  
1019 **suggesting lower complex stability.** CL4 cell co-expressing CDHR2-Halo (magenta)  
1020 and CDHR5-EGFP (green) photobleached at a medial ROI; 15s and 30s intervals shown.  
1021 Scale bar: 5  $\mu$ m.

1022

1023 **Video S4: Marginal homophilic CDHR2 adhesion complexes have higher signal**  
1024 **recovery, suggesting lower complex stability.** Mixed CL4 cells expressing CDHR2-  
1025 EGFP (green) and CDHR2-mCherry (magenta) photobleached at a marginal ROI; 15s  
1026 intervals shown. Scale bar: 5  $\mu$ m.

1027

1028 **Video S5: Marginal homophilic CDHR5 adhesion complexes have higher signal**  
1029 **recovery, suggesting lower complex stability.** Mixed CL4 cells expressing CDHR5-  
1030 EGFP (green) and CDHR5-mCherry (magenta) photobleached at a marginal ROI; 30s  
1031 intervals shown. Scale bar: 5  $\mu$ m.

1032

1033 **Video S6: Microvilli accumulate first at cell margins over cell surface**  
1034 **differentiation.** (Left) CL4 cells expressing mCherry-ESPN imaged at 3-minute intervals  
1035 for 43 hours. (Right) Fire LUT intensity profile of the ESPN channel. Intensity scales from

1036 low (0; dark purple) to high (255; yellow/white) as denoted by LUT profile. StackReg  
1037 ImageJ plugin was used to align all frames of the movie. Scale bar: 10  $\mu$ m.  
1038